

Small-Scale Wind Fluctuations in the Tropical Tropopause Layer from Aircraft Measurements: Occurrence, Nature, and Impact on Vertical Mixing

AURÉLIEN PODGLAJEN,^a T. PAUL BUI,^b JONATHAN M. DEAN-DAY,^b LEONHARD PFISTER,^b
 ÉRIC J. JENSEN,^b M. JOAN ALEXANDER,^c ALBERT HERTZOG,^d BERND KÄRCHER,^e
 RIWAL PLOUGONVEN,^f AND WILLIAM J. RANDEL^g

^a *Laboratoire de Météorologie Dynamique, CNRS-UMR8539, Institut Pierre Simon Laplace, École Normale Supérieure, École Polytechnique, Université Pierre et Marie Curie, Paris, France*

^b *NASA Ames Research Center, Moffett Field, California*

^c *CoRA Office, NorthWest Research Associates, Boulder, Colorado*

^d *Laboratoire de Météorologie Dynamique/IPSL, UPMC University Paris 06, CNRS, Palaiseau, France*

^e *Institut für Physik der Atmosphäre, Deutsches Zentrum für Luft- und Raumfahrt, Wessling, Germany*

^f *Laboratoire de Météorologie Dynamique/IPSL, École Polytechnique, Paris-Saclay University, Palaiseau, France*

^g *National Center for Atmospheric Research, Boulder, Colorado*

(Manuscript received 11 January 2017, in final form 31 May 2017)

ABSTRACT

The contribution of turbulent mixing to heat and tracer transport in the tropical tropopause layer (TTL) is poorly constrained, partly owing to a lack of direct observations. Here, the authors use high-resolution (20 Hz) airborne measurements to study the occurrence and properties of small-scale (<100 m) wind fluctuations in the TTL (14–19 km) over the tropical Pacific. The fluctuations are highly intermittent and appear localized within shallow (100 m) patches. Furthermore, active turbulent events are more frequent at low altitude, near deep convection, and within layers of low gradient Richardson number. A case study emphasizes the link between the turbulent events and the occurrence of inertio-gravity waves having small horizontal or vertical scale. To evaluate the impact of the observed fluctuations on tracer mixing, their characteristics are examined. During active events, they are in broad agreement with inertial-range turbulence theory: the motions are close to 3D isotropic and the spectra follow a $-5/3$ power-law scaling. The diffusivity induced by turbulent bursts is estimated to be on the order of $10^{-1} \text{ m}^2 \text{ s}^{-1}$ and increases from the top to the bottom of the TTL (from $\sim 2 \times 10^{-2}$ to $\sim 3 \times 10^{-1} \text{ m}^2 \text{ s}^{-1}$). Given the uncertainties involved in the estimate, this is in reasonable agreement (about a factor of 3–4 lower) with the parameterized turbulent diffusivity in ERA-Interim, but it disagrees with other observational estimates from radar and radiosondes. The magnitude of the consequent vertical transport depends on the altitude and the tracer; for the species considered, it is generally smaller than that induced by the mean tropical upwelling.

1. Introduction

The tropical tropopause layer (TTL; Fueglistaler et al. 2009) is the transition region between the convectively influenced tropical troposphere and the radiatively controlled tropical lower stratosphere. Hence, constituents in the TTL are believed to be vertically transported either by deep convection carrying air from the boundary layer or by the mean tropical upwelling associated with the lower branch of the Brewer–Dobson circulation. Similarly, latent heat release (negligible

above 14–15 km) and radiative heating dominate the heat balance of the tropical upper troposphere–lower stratosphere (UTLS), at least in reanalyses (Wright and Fueglistaler 2013). However, for both the heat (Wright and Fueglistaler 2013) and the tracer budget (Mote et al. 1996, 1998), the effect of turbulent mixing and diffusion is highly uncertain. It might have a significant influence on the thermal and wind structure of the TTL (Flannaghan and Fueglistaler 2014), on its water vapor and ice content (Bardeen et al. 2013; Ueyama et al. 2015), or on the vertical transport through that layer to the stratosphere (Konopka et al. 2007). Given the very slow mean upwelling (about 0.2 mm s^{-1} at 80 hPa), even weak turbulent mixing could indeed be sufficient to

Corresponding author: Aurélien Podglajen, aurelien.podglajen@lmd.polytechnique.fr

compete with advection. The uncertainty on the magnitude of turbulent diffusion limits our understanding of TTL processes and is a problem when modeling its composition. This uncertainty comes from the computational unfeasibility of direct numerical simulations of turbulence and its generation processes in the TTL, from the low level of theoretical understanding of turbulence generation, nature, and life cycle, but it is also due to a lack of measurements of small-scale fluctuations.

Indeed, most estimates of turbulent diffusivity come from radar or balloon measurements at specific tropical locations (Rao et al. 2001; Alappattu and Kunhikrishnan 2010). Turbulence intensity can be measured from commercial airplanes (Cornman et al. 1995, 2004), and a fleet is now equipped to provide quantitative estimates (Sharman et al. 2014). However, the sampling is still sparse outside the continental United States, and, in any case, those aircraft fly below the bottom of the TTL (14 km). At higher altitudes, precise measurements of meteorological parameters and turbulence have been carried out in the past on board scientific aircraft measuring platforms (e.g., Lilly et al. 1974; Chan et al. 1998; Koch et al. 2005) but very few (and all unpublished to our knowledge) took place in the TTL. Recently, during the NASA Airborne Tropical Tropopause Experiment (ATTREX) campaign (boreal winters 2013 and 2014), such measurements were acquired between 14 and 19 km over the tropical Pacific, providing a unique opportunity to quantify turbulence in the TTL.

In this work, we use the meteorological measurements from ATTREX to characterize the nature and occurrence of small-scale wind fluctuations in the TTL. The paper is organized as follows. Section 2 introduces the ATTREX campaign and the data used. Then, in section 3, a specific case study is presented to illustrate the measured small-scale fluctuations and their relationship with waves. Next, we provide a systematic examination of the statistics and context of small-scale fluctuations occurrence in the whole dataset (section 4). In section 5, the characteristics of small-scale fluctuations are studied and compared with theoretical expectations for inertial-range turbulence (isotropy, power-law scaling). Finally, section 6 presents an estimate of the turbulent diffusivity from aircraft observations and compares it with estimates derived from other measurements and the values used in modern reanalyses systems. The results and conclusions are summarized in section 7.

2. Data and methods

a. Presentation of ATTREX campaign and MMS measurements

During the ATTREX campaign in boreal winters 2013 and 2014, the NASA Global Hawk unmanned

aircraft flew through the tropical tropopause layer (14–19 km) (Jensen et al. 2017). It sampled the central and eastern Pacific in February–March 2013 from California and the western Pacific in February–March 2014 from Guam. A map of all flights is displayed in Fig. 1. Combining both years, a reasonable sampling of the tropical Pacific region was achieved, with more data in the northern tropics. Since both 2013 and 2014 were nearly neutral ENSO years, the fact that the measurements were carried out one year apart (2013 vs 2014) is probably of second order compared to the difference in geographic location (eastern Pacific vs convective western Pacific). This is confirmed by comparing the distribution of Richardson numbers from radiosonde observations in the western Pacific between the two years (not shown).

Small-scale fluctuations are analyzed using ATTREX Meteorological Measurement System (MMS) data (Scott et al. 1990), which includes 3D wind, temperature, and pressure recorded at a frequency of 20 Hz (dataset produced by Bui et al. 2014). The winds are deduced from the measured pitch, roll, and heading of the aircraft and from differential pressure sensors appropriately located on the aircraft fuselage (Scott et al. 1990). The reported sensor precisions are 0.1 m s^{-1} for the longitudinal (along-flight track) horizontal wind u_l and 0.05 m s^{-1} for the vertical and horizontal transverse to flight-track winds w and u_t . The different precisions between u_l on the one hand, and u_t and w on the other hand, mainly arise at high frequencies: the forward (ram) pressure sensor used to estimate u_l needs to accommodate the large pressure value associated with the aircraft's high true airspeed, so that it is less sensitive to the small-amplitude fluctuations at high frequencies than the differential pressure sensors used to measure u_t and w . Hence, quantitative observations of small scales mainly rely on the high-frequency measurements of u_t and w .

The temperature sensor has a precision of 0.05 K while the pressure sensor precision is 0.3 Pa. Since we are interested in the very high frequencies ($>1 \text{ Hz}$), the temperature sensor response time has a substantial impact. In the flight conditions of ATTREX, the response time of the Rosemount temperature sensor is estimated to be typically 200–400 ms, so that it affects high-frequency measurements. Because of remaining uncertainties in the detailed high-frequency response of the sensor in flight conditions, only limited quantitative use of the temperature data is made in the paper.

b. Coordinate of the measurements and Taylor's hypothesis

Wind, temperature, and pressure observations are recorded as a function of time along the plane trajectory. However, as emphasized by Bacmeister et al. (1996),

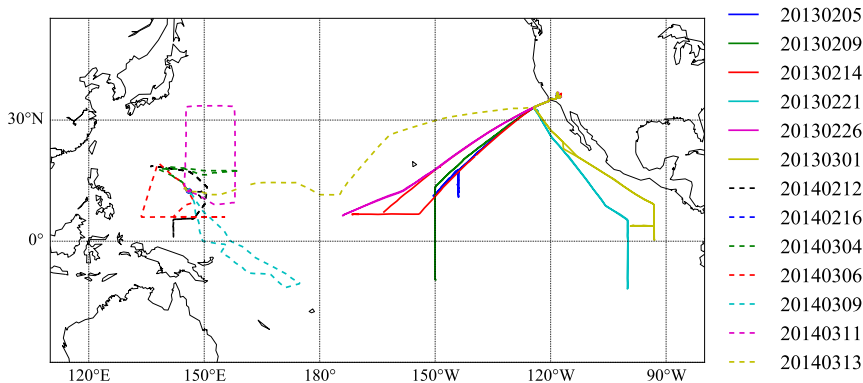


FIG. 1. Map of all ATTREX flights used in this study. Eastern Pacific flights were carried out in February–March 2013, while western Pacific ones flew in February–March 2014.

they should be interpreted as instantaneous sections along the spatial coordinate of the aircraft position. For turbulence, the approximation holds when the plane speed is much larger than the wind speed. In this case, the determination of the spatial coordinate can be refined and extended using the measured true airspeed (TAS)—that is, the air motion relative to the aircraft. The correction relies on Taylor’s “frozen turbulence hypothesis,” which states that small turbulent eddies are stationary following the flow; that is, they are just advected by the background wind and larger eddies.

In the paper, we assume Taylor’s hypothesis and use the TAS to convert time scale to spatial scale. The Global Hawk TAS generally exceeds the ground relative wind speed by a factor of 5, and the TAS does not vary much during the flights so that our methodology is similar to analyzing the observations in time with a constant TAS of about $170\text{--}180\text{ m s}^{-1}$ or directly in (ground relative) horizontal position. Since they only marginally affect the high frequencies, the variations of the heading of the aircraft and its vertical ascent rate relative to the horizontal speed are neglected.

c. Wavelet analysis and estimation of high-frequency variance and eddy dissipation rates

As will be shown later in the paper, the small-scale fluctuations in wind and temperature are intermittent: aircraft observations show periods of high and low activity at high frequency. To quantify how activity at various frequencies varies with time, we used a continuous wavelet transform (e.g., Torrence and Compo 1998) to perform time–frequency decomposition of the small-scale fluctuations.

In practice, we used a Morlet mother wavelet, applied in the time coordinate of the measurements. We retain the high frequencies (2–10-Hz band; i.e., up to the Nyquist frequency) of the wavelet transform to compute the

evolution of the high-frequency wind or temperature variance σ_{HF}^2 . Further discussion can be found in appendix A.

The eddy dissipation rate of kinetic energy ε_k is often used rather than the wind variance to quantify the intensity of small-scale motions (e.g., Wilson 2004), specifically with the form $\varepsilon_k^{1/3}$ (the “EDR”) in the aviation turbulence literature (Sharman et al. 2014). Following previous studies (e.g., Lilly et al. 1974; Chan et al. 1998), we derive ε_k assuming that the power spectral densities of the longitudinal velocity component Φ_{u_l} and of the vertical and transverse (normal to track) components Φ_w and Φ_{u_t} , follow Kolmogorov $\kappa^{-5/3}$ spectra:

$$\begin{aligned} \Phi_{u_l}(\kappa) &= \alpha_k \varepsilon_k^{2/3} \kappa^{-5/3} \quad \text{and} \\ \Phi_w(\kappa) = \Phi_{u_t}(\kappa) &= \frac{4}{3} \alpha_k \varepsilon_k^{2/3} \kappa^{-5/3}, \end{aligned} \quad (1)$$

where κ is the along-track angular wavenumber (rad m^{-1}) and α_k is the “universal” Kolmogorov constant for high-Reynolds-number flows. A common value is $\alpha_k \simeq 0.5$, suggested, for example, by Sreenivasan (1995). To estimate ε_k , we use only the two transverse wind components, u_t and w , since u_l measurements are less sensitive to high-frequency fluctuations. Two estimates of ε_k are derived separately from the w and u_t variances integrated over the wavenumber range $[\kappa_1 - \kappa_2]$:

$$\begin{aligned} \varepsilon_w &= \left[\frac{\int_{\kappa_1}^{\kappa_2} \Phi_w(\kappa) d\kappa}{2\alpha_k(\kappa_1^{-2/3} - \kappa_2^{-2/3})} \right]^{3/2} \quad \text{and} \\ \varepsilon_{u_t} &= \left[\frac{\int_{\kappa_1}^{\kappa_2} \Phi_{u_t}(\kappa) d\kappa}{2\alpha_k(\kappa_1^{-2/3} - \kappa_2^{-2/3})} \right]^{3/2}, \end{aligned} \quad (2)$$

where $\int_{\kappa_1}^{\kappa_2} \Phi_{w,u_i}(\kappa) d\kappa = (\sigma_{\text{HF}}^2)_{w,u_i}$ is the estimate of the high-frequency variance. In practice, $\kappa_1 = 2\pi f_1/V_a$ and $\kappa_2 = 2\pi f_2/V_a$, where V_a is the true airspeed and $f_1 = 2$ Hz and $f_2 = 10$ Hz; assuming $V_a \simeq 180 \text{ m s}^{-1}$, our frequency bounds f_1 and f_2 correspond to frozen wavelengths of 90 and 18 m. The “true” ε_k is then estimated as the geometric mean of the estimates from w and from u_i :

$$\varepsilon_k = \sqrt{\varepsilon_w \varepsilon_{u_i}}. \quad (3)$$

The noise level on ε_k arising from instrumental and quantization noise in the wind speed measurement is estimated to be around $10^{-7} \text{ m}^2 \text{ s}^{-3}$. No value can be measured below that noise level. The resolution is better than 1 s, and the instantaneous sampling precision is about 50% and drops below 25% for the 1-s average.

It is important to note that, strictly speaking, the expressions for the wind spectra in Eq. (1) are valid for small-scale turbulence in the so-called inertial range. While the ATTREX MMS measurements can resolve a wide range of turbulent motions, they resolve the inertial range only during the strongest turbulent bursts; for weaker turbulent bursts the resolved motions are likely to be impacted by buoyancy effects. Indeed, several authors (e.g., Weinstock 1978a) have proposed that the upper bound of the inertial range, the scale above which buoyancy effects are sufficiently large to significantly impact the motions, called the outer scale L_m , be related to the Ozmidov scale:

$$L_O = \sqrt{\frac{\varepsilon_k}{N^3}} \quad (4)$$

(where N is the Brunt–Väisälä frequency) through

$$L_m = \frac{2\pi}{C} L_O = \frac{2\pi}{C} \sqrt{\frac{\varepsilon_k}{N^3}}. \quad (5)$$

Weinstock (1978b) proposed a value $C = 0.62$ for the dimensionless C constant, although later Weinstock (1992) argued that C may actually be variable, while Lindborg (2006) suggested different transition scales L_m in the horizontal and vertical spectra. With $C = 0.62$ in Eq. (5), L_m can be expressed as

$$L_m \simeq 10 L_O = 10 \sqrt{\frac{\varepsilon_k}{N^3}}. \quad (6)$$

As discussed below, ε_k may vary between 10^{-8} and $10^{-2} \text{ m}^2 \text{ s}^{-3}$ in the TTL, whereas $N \simeq 1 - 2 \times 10^{-2} \text{ rad s}^{-1}$. Hence, L_m may vary from less than 0.5 m to more than 500 m. For $\varepsilon_k \geq \varepsilon_{\text{lim}} = 10^{-3} \text{ m}^2 \text{ s}^{-3}$, corresponding to strong turbulent bursts, $L_m \geq 110 \text{ m}$ and ATTREX

measurements might partly resolve inertial-range turbulence. Then, ε_k from Eqs. (2) and (3) is an estimate of the actual eddy dissipation rate of kinetic energy. However, for smaller values of ε_k , the measurements generally do not fully resolve inertial-range turbulence, and our estimate of ε_k might differ from actual kinetic energy eddy dissipation rates. Only dedicated high-resolution instruments are able to measure the eddy dissipation rate in weakly turbulent regions (e.g., Balsley 2008; Theuerkauf et al. 2011; Schneider et al. 2015). In this paper, ε_k is always derived using Eqs. (2) and (3) using scales between about 18 and 90 m and may be considered as an estimate of the eddy dissipation rates only for its largest values. Some confidence in the reported values of ε_k is provided by the fact that changing the frequency bounds from $f_1 = 2$ Hz and $f_2 = 10$ Hz to $f_1 = 1$ Hz and $f_2 = 5$ Hz only marginally affects the results quantitatively (by less than 50%), while leaving the qualitative conclusions unchanged.

3. A case study of small-scale fluctuation occurrence

Because of a failure of the communications system for command and control, the Global Hawk remained within 2° of Guam ($13^\circ 30' \text{ N}$, $144^\circ 48' \text{ E}$) during the second flight of ATTREX 2014 (16 February 2014). The aircraft track for this specific flight is shown in Fig. 2. Twenty-six vertical profiles were acquired during that flight, allowing a precise documentation of the local TTL vertical wind and thermal structure (Kim 2015), and of the repartition of small-scale fluctuations. We examine the distribution of ε_k measurements and their repartition in the tropical tropopause layer during this well-documented period.

Figure 3 shows the time–altitude profiles of temperature and meridional and zonal winds and eddy dissipation rates. A low-frequency inertio-gravity wave pattern can be identified through coherent vertical oscillations in the wind and temperature fields, and the different phases of the oscillations are indicated by the black lines. A slow descent of the wave phase during the flight can also be noticed, but overall the wave structure remained essentially stationary.

Figure 4 shows all vertical profiles of meridional wind V and potential temperature θ from that same flight. As expected, it is apparent that the wave produces structures in the stability $\partial\theta/\partial z$ and the vertical shear $(\partial\bar{u}/\partial z)^2 + (\partial\bar{v}/\partial z)^2$; it could thus drive dynamic instabilities, such as Kelvin–Helmholtz instability and structure turbulence occurrence (e.g., Fritts et al. 2009). Indeed, in Fig. 3, the profiles of ε_k show sporadic turbulence in the lower part of the TTL, but above 15.5 km

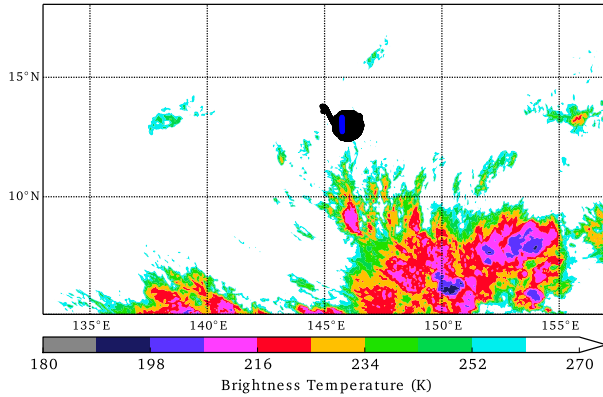


FIG. 2. ATTREX flight track on 16–17 Feb 2014 (black), when the Global Hawk remained near Guam. The brightness temperature of the MTSAT window channel at 0500 UTC 17 Feb is shown by the color scale and indicates the location of high-altitude clouds. The location of the flight section presented in Fig. 5 is shown in blue.

the high ε_k appear regrouped in two layers: one around 17 km active between 26 and 32 h, and a weaker one at 16.2 km mainly active between 23 and 26 h.

Figure 4 shows the mean gradient Richardson number Ri_g profile induced by the wave and the frequency of occurrence of turbulence as a function of altitude during the flights. We define Ri_g by

$$Ri_g = \frac{N^2}{\left(\frac{\partial \bar{u}}{\partial z}\right)^2 + \left(\frac{\partial \bar{v}}{\partial z}\right)^2}, \quad (7)$$

where $N^2 = (g/\bar{\theta}) (\partial \bar{\theta} / \partial z)$ ($g = 9.81 \text{ m s}^{-2}$). Consistent with expectations from shear instabilities, Fig. 4 shows that high ε_k values tend to be more frequent in the regions of low mean Richardson number, although the correspondence is not one to one owing to the use of an average wind profile to compute Ri_g here.

Thus, Fig. 4 demonstrates that low-frequency, small vertical wavelength (on the order of 2 km or less) waves play a key role in creating instabilities and enhancing the occurrence of turbulence in the tropics, as was already anticipated from the analysis of earlier aircraft observations by Pfister et al. (1986). Since equatorial waves with short vertical scales are often underestimated in current meteorological analyses and re-analyses (Podglajen et al. 2014; Kim and Alexander 2015), which have typical vertical resolution of 0.7 km at the most in the TTL, the finescale vertical structure of turbulence is probably missed by global weather and climate models.

Besides the direct modulation of shear and stability, the large-scale IGW also provides a background state in which shorter-scale, higher-frequency gravity waves propagate. Small-scale waves might also contribute to

generating turbulence (Pellacani and Lupini 1975; Lane et al. 2012). Figure 5 shows that, before entering the turbulent layer near 17 km, the aircraft flew through a well-defined monochromatic gravity wave packet of wavelength < 10 km (seen as consistent oscillations in potential temperature and vertical wind). However, it is difficult to demonstrate a connection between this gravity wave and the onset of turbulence from the observations only.

Nevertheless, this case study shows that fine-scale (vertical or horizontal) waves, which are unresolved in current global models, are important contributors to the driving of turbulence. Since a major source of gravity waves in the tropics is deep convection, this also suggests an important role of convectively induced (clear air) turbulence in the TTL. We will explore the influence of deep convection on turbulence occurrence in the next section.

4. Statistics of turbulence occurrence over the tropical Pacific during ATTREX

The previous section emphasized the role of gravity waves on small-scale fluctuations occurrence. This section systematically examines the relationship between small-scale wind fluctuations and their environment.

a. Definition of active events; distribution of ε_k during all ATTREX flights

Figure 6 shows the distribution of ε_k for all ATTREX flights, as well as for specific regions and altitude ranges. The values below the instrumental noise level ($10^{-7} \text{ m}^2 \text{ s}^{-3}$; see appendix B) are not shown. However, the highest branches of the distributions are well above the noise and vary by several orders of magnitude: typical values of ε_k hence range from below 10^{-7} to a few $10^{-1} \text{ m}^2 \text{ s}^{-3}$. We note that, even for the lowest of those typical values, the observed scale range (scales larger than 10 m) is well above the dissipation range starting below the Kolmogorov scale l_ν , which depends on the eddy dissipation rate ε_k and on the molecular viscosity ν : $l_\nu = (\nu^3/\varepsilon_k)^{1/4}$. In typical TTL conditions, $l_\nu \ll 1$ m.

Figure 6 displays ε_k distribution in the eastern–central Pacific (ATTREX 2013) and western Pacific (ATTREX 2014) and in the lower (below 15.5 km) and upper (above 15.5 km) TTL. High ε_k are more frequently observed over the convective western Pacific than the eastern Pacific, and they are generally more frequent in the lower TTL. For all the distributions, the high ε_k tail resembles a lognormal distribution, which is consistent with radar (e.g., Wilson et al. 2005) or other aircraft observations (e.g., Sharman et al. 2014) and with direct numerical simulations of turbulence generated by wave breaking (Fritts et al. 2009).

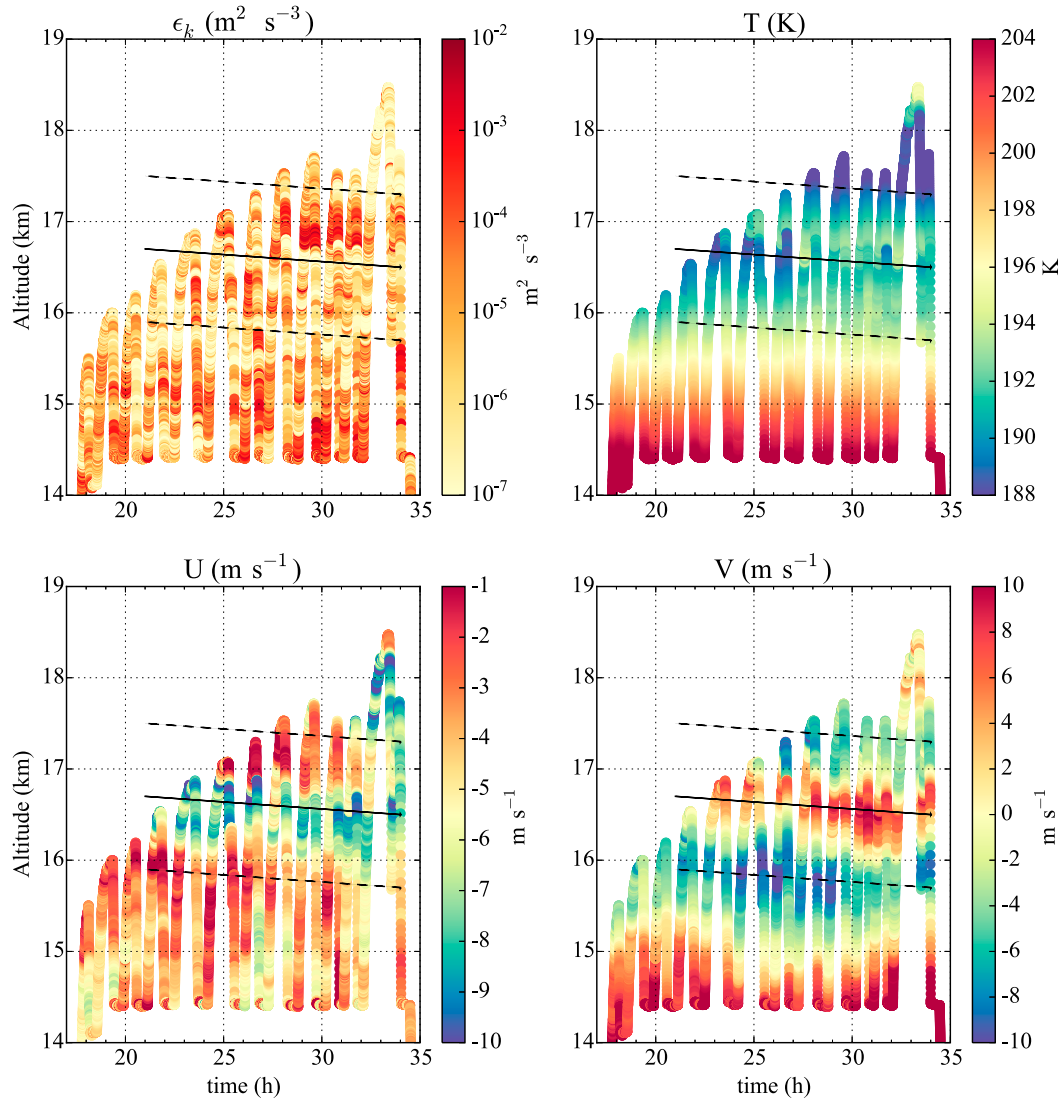


FIG. 3. On 16 Feb 2014, time–altitude profiles of (top left) eddy dissipation rate ϵ_k [estimated from the measured vertical and transverse winds w and u_t using Eqs. (2) and (3)], (top right) temperature, (bottom left) zonal wind, and (bottom right) meridional wind from aircraft observations showing the relationship of active layers with larger-scale shear associated with an inertio-gravity wave. The black lines emphasize the different wave phases of the inertio-gravity wave: dashed lines correspond to negative meridional wind V anomalies due to the wave, whereas the continuous line corresponds to the positive meridional wind anomaly in the bottom-right panel. The same lines have been added to the other panels in order to guide the eye in spotting the inertio-gravity wave structure in U and T and its impact on high- ϵ_k layers.

The vertical black line in Fig. 6 corresponds to the threshold chosen to define “active” events. A measurement is considered to be part of an active event if its ϵ_k rate is above a threshold of $\epsilon_{\text{lim}} = 10^{-3} \text{ m}^2 \text{ s}^{-3}$. This threshold (equivalent to $\text{EDR} = \epsilon_k^{1/3} = 0.1 \text{ m}^{2/3} \text{ s}^{-1}$) is similar in magnitude to thresholds taken to classify aviation turbulence (Sharman et al. 2014). The fact that the different curves in Fig. 6 do not intersect each other for $\epsilon_k \geq 10^{-4} \text{ m}^2 \text{ s}^{-3}$ suggests that the characterization of the environment of the active bursts will not be strongly

sensitive to the threshold used to isolate them. Indeed, using different thresholds does not qualitatively affect the results.

b. Distribution of small-scale fluctuations with altitude and Richardson number

As seen in the Guam case study, turbulence occurrence is related to shear and stability variations. In the TTL, both the stability and the shear strongly increase with altitude, at least over the tropical Pacific. They tend

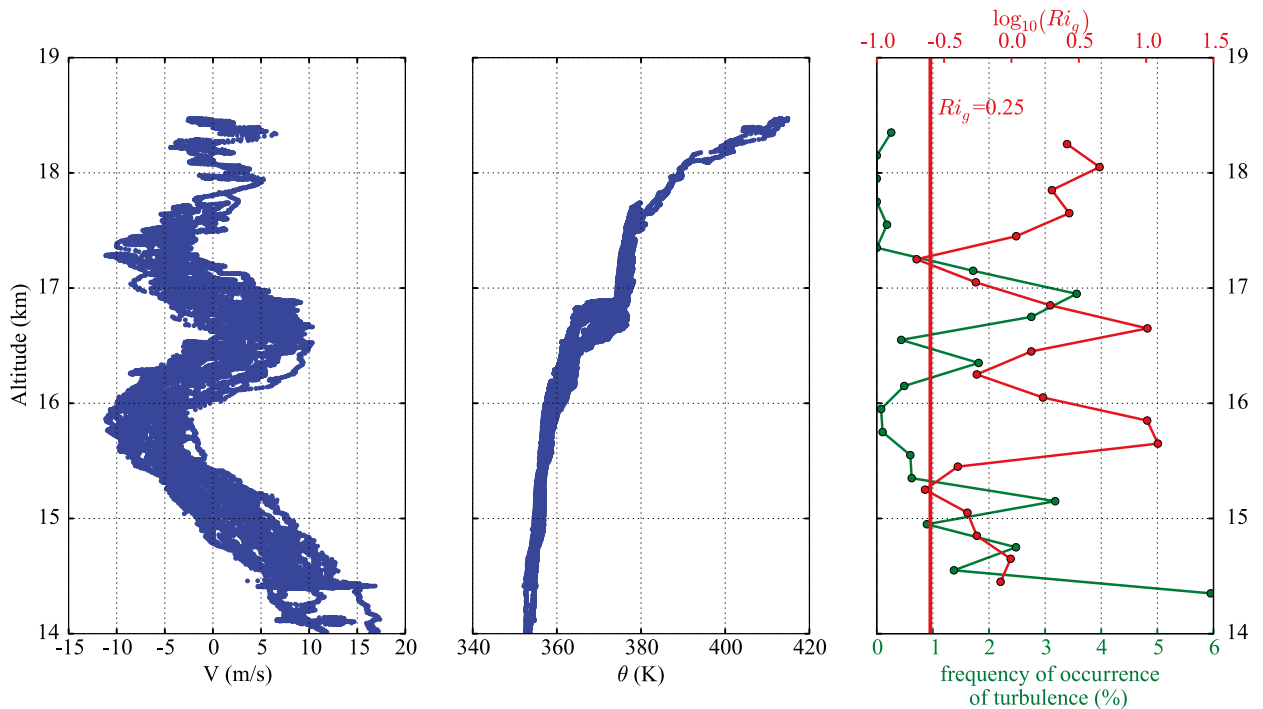


FIG. 4. Profiles of (left) meridional wind V , (middle) potential temperature θ , and (right) Ri_g (red) and turbulence occurrence frequency (green), from the flight on 16 Feb 2014 during which the Global Hawk stayed near Guam (within 2°). The gradient Richardson number Ri_g and turbulence occurrence are estimated from all the average of the 26 profiles acquired on that day.

to balance one another, so that the distribution of the gradient Richardson number Ri_g does not vary too much with altitude, as indicated by radiosonde measurements (not shown; see also Fig. 4). The stability effect is nevertheless dominant, so that the typical Ri_g slightly increases with altitude in the TTL. For this reason and because turbulence generating processes, such as deep convection, are more active in the lower TTL, turbulence occurrence is expected to depend on altitude. Figure 7 shows the profile of occurrence frequency of active events as a function of altitude in the whole dataset and for the eastern and western tropical flights separated. The vertical profiles show different behaviors, with a strong increase below 15 km in the tropical western Pacific whereas in the eastern Pacific turbulence occurrence seems to peak around 16-km altitude and then decreases when approaching the stratosphere. The frequency of turbulence occurrence is higher in the western Pacific than in the eastern Pacific at all altitudes, but we note that the difference is not so dramatic above about 15.5 km.

The flight strategy used in ATTREX was such that most of the time the Global Hawk was climbing and descending through the TTL (see Fig. 3). During climbs, the horizontal speed of the aircraft is much larger than its vertical ascent rate so that it is generally difficult to

derive local estimates of the shear or of the Richardson number at the aircraft position. However, during descents, the vertical speed is larger (generally about $4\text{--}5\text{ m s}^{-1}$). In the stratified TTL, descents can then be used to estimate the background wind vertical shear. We used 200-m vertical segments from the descents to obtain collocated measurements of the large-scale Ri_g and of turbulence occurrence frequency. Figure 8 shows the frequency distribution of the Richardson number from the about 2000 segments of 200 m (blue curve). Highly stable layers are frequent, and the most frequent Ri_g are observed between 0.25 (the onset of Kelvin–Helmholtz instability) and 1 (threshold for turbulence to be maintained). Rare occurrences of Ri_g below 0.25 are found (about 12%), and about 3% show slightly negative N^2 ; those might not be strictly negative, since the soundings are not strictly vertical and in the case of low positive N^2 the small horizontal temperature gradients can affect this value. Figure 8 also shows the frequency of occurrence of turbulence as a function of Ri_g . As expected, turbulence is more frequent for low Richardson numbers, with the occurrence frequency reaching about 10% for very low Ri_g (below 0.1). It should be noted here that the choice of the scale at which to calculate the wind shear and temperature lapse rate is somewhat arbitrary, as well as the threshold taken to select turbulent events,

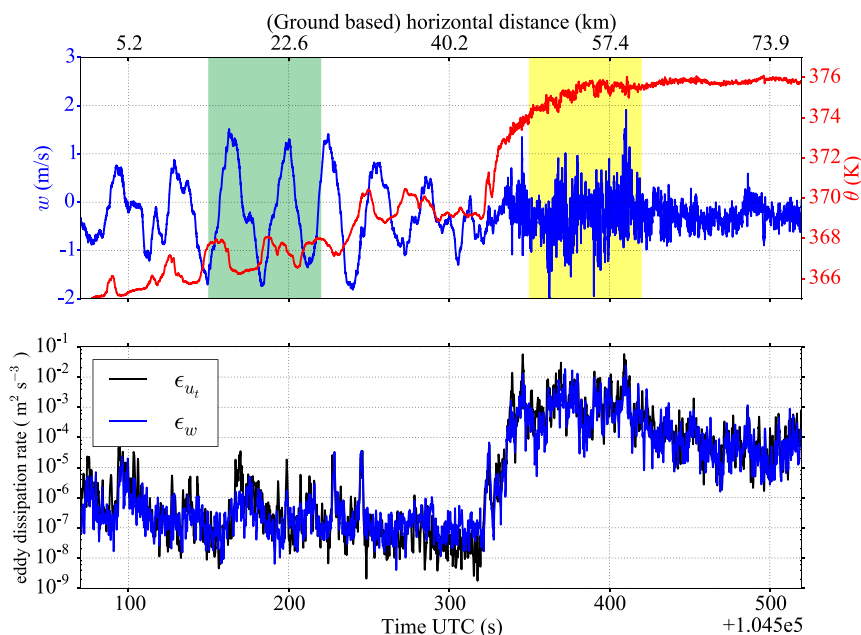


FIG. 5. (top) Time series of vertical wind w (m s^{-1}) and potential temperature θ (K) along an aircraft climb on 16 Feb 2014 near Guam. This is the same flight as shown (entirely) in Fig. 4, but for a short period around time 29 h, near the turbulent layer at about 17 km. A quiet period and a period with active small-scale fluctuations are emphasized with green and yellow backgrounds, respectively. (bottom) For the same time segment, time series of eddy dissipation rate of kinetic energy from vertical wind only (blue) and from transverse horizontal wind only (black).

so that this figure should be taken as merely qualitative and illustrative of the effect of the background shear and stability. (We note that choosing another scale to compute Ri_g does not change the result qualitatively although there are some quantitative differences.) As emphasized in the case study, fine vertical-scale waves modulate this vertical shear and stability.

c. Relationship between turbulence in the TTL and deep convection

The increased occurrence of turbulence in the vicinity (but out of) convective clouds has been the subject of much research owing to the subsequent hazard it creates for aviation (Lane et al. 2012). It is often named convectively induced turbulence (CIT) in this context. As emphasized by the Guam case study, convectively generated gravity waves are one of the processes linking turbulence to convective clouds. Thanks to the extended area sampled during ATTREX, it is possible to examine the effect of convection on an unprecedented spatial scale. Convection is here determined by examining the brightness temperature in the $10.8\text{-}\mu\text{m}$ infrared window channel in the nearest-in-time geostationary image collected every 30 min by the Japanese Multifunctional Transport Satellites (MTSAT) or by the American

Geostationary Operational Environmental Satellite-West (GOES-West). A pixel (about $4\text{ km} \times 4\text{ km}$) is considered convective if its brightness temperature T_b is lower than 235 K, following Liu et al. (2007). We note that the results are not overly sensitive to the choice of this T_b threshold. Figure 9 shows that, in the vicinity of convection, turbulence occurrence strongly increases. This is especially true at low altitudes (14–15.5 km) where the occurrence frequency can reach 8% or so, but at higher altitudes the data also follow this pattern. Since in the western Pacific convection is more frequent than in the eastern Pacific, Fig. 9 is consistent with Fig. 7, which showed more frequent turbulence over the eastern Pacific, especially in the lower TTL. Figure 9 is similar in essence to Fig. 3 in Lane et al. (2012), who showed that distance to convection also controlled the distribution of turbulence occurrence in the UTLS but at a much finer scale (tens of kilometers). This figure suggests that deep convection is a key factor controlling (clear sky) turbulence occurrence in the TTL. A number of studies (e.g., Lane and Sharman 2006) have emphasized the role of convectively generated gravity waves as a link between deep convection and clear-air turbulence, through the enhancement of instabilities. Gravity wave activity is indeed generally enhanced near cold

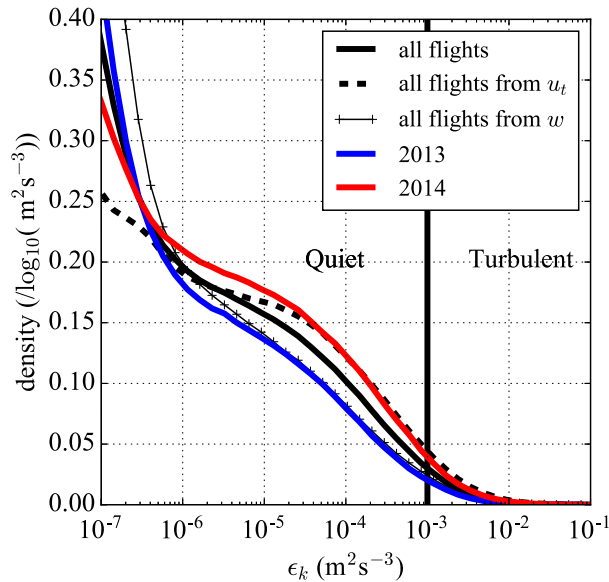


FIG. 6. PDF of ϵ_k for all ATTREX flights estimated from u_t only (dashed black line) and from w only (crosses) or using Eq. (3) (continuous black line), 2013 eastern Pacific flights (blue line), and 2014 western Pacific flights (red line). The vertical black line shows the threshold chosen to select occurrence of active events. Only the values above the estimated noise level ($\sim 1 \times 10^{-7} \text{ m}^2 \text{ s}^{-3}$) are shown.

convective cloud tops (Alexander et al. 2000). Consistent with that picture, Fig. 8 shows that low Ri_g values, probably associated with wave activity are more frequent in the vicinity of convection.

In addition to the relationship with convection, past studies have reported enhanced turbulence within thick midlatitude cirrus (e.g., Gultepe and Starr 1995; Chan et al. 1998). During ATTREX, different relationships between clouds and turbulence were observed depending on the altitude and geographic location. In general, no correlation between thin TTL cirrus and turbulence was found in the upper part of the flights (above 15 km) but there were more occurrences of strong small-scale fluctuations within cirrus in the western Pacific lower TTL (not shown). This suggests that the existence of enhanced turbulence within cirrus depends on cloud properties and their environment, similar to the impact of in-cloud radiative heating on cirrus evolution (Jensen et al. 2011; Podglajen et al. 2016b). Systematic examination of the cirrus–turbulence relation will be the subject of a dedicated follow-up study.

5. Nature of the small-scale fluctuations

Small-scale motions encountered in the UTLS are generally referred to as turbulence. Such a framing implicitly brings to mind the Kolmogorov inertial range,

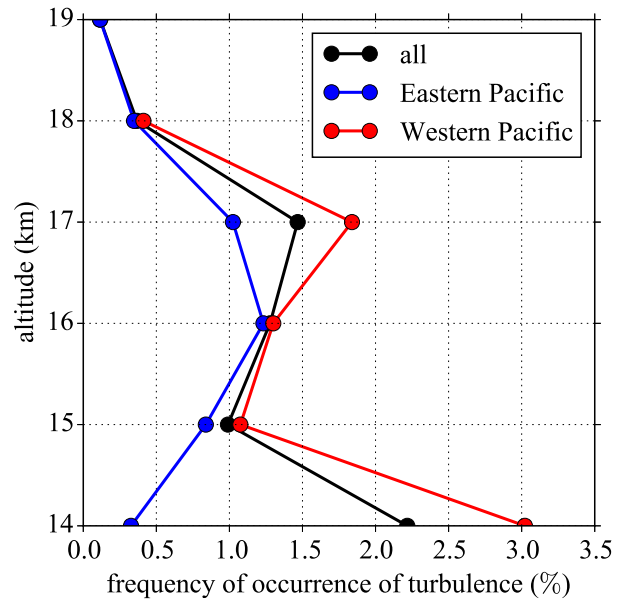


FIG. 7. Occurrence frequency of turbulence (defined by $\epsilon_k \geq 10^{-3} \text{ m}^2 \text{ s}^{-3}$) as a function of altitude, for all ATTREX flights (black) and in the eastern Pacific (boreal winter 2013; blue) and western Pacific (boreal winter 2014; red). The frequency is computed from all observations within 1-km layers.

but the exact nature of the observed motions, gravity waves or turbulence, is not always clear. This probably does not matter for aircraft safety, and in that context, all fluctuations in the $\sim 10 \text{ m}–2 \text{ km}$ scale range perturbing commercial aircraft flights might be named “turbulent” (Lane et al. 2012). However, knowledge of the nature of the fluctuations is important for estimating their impact on mixing.

Part of the uncertainty comes from the fact that an approximate $k^{-5/3}$ spectrum is present on a wide range of scales from the mesoscale (hundreds of kilometers; Nastrom and Gage 1985) to the very microscale (a few meters) and that its nature at the mesoscale is still debated (e.g., Lilly 1983; Gage et al. 1986; Bacmeister et al. 1996; Lindborg 1999; Callies et al. 2014). The sub-100-m-scale motions examined here are better understood: as emphasized in section 2, they might be similar to inertial-range turbulence when the outer scale L_m of the inertial range is sufficiently large—that is, when ϵ_k is sufficiently large. For scales larger than L_m , however, stratification and buoyancy forces are believed to have a more significant role in shaping the dynamics (Weinstock 1978a; Lumley 1964), and the inertial-range hypotheses (e.g., isotropic motions) are probably not verified. In this section, we examine the characteristics of the sub-100-m motions during high ϵ_k bursts and their broad consistency with inertial-range turbulence theory.

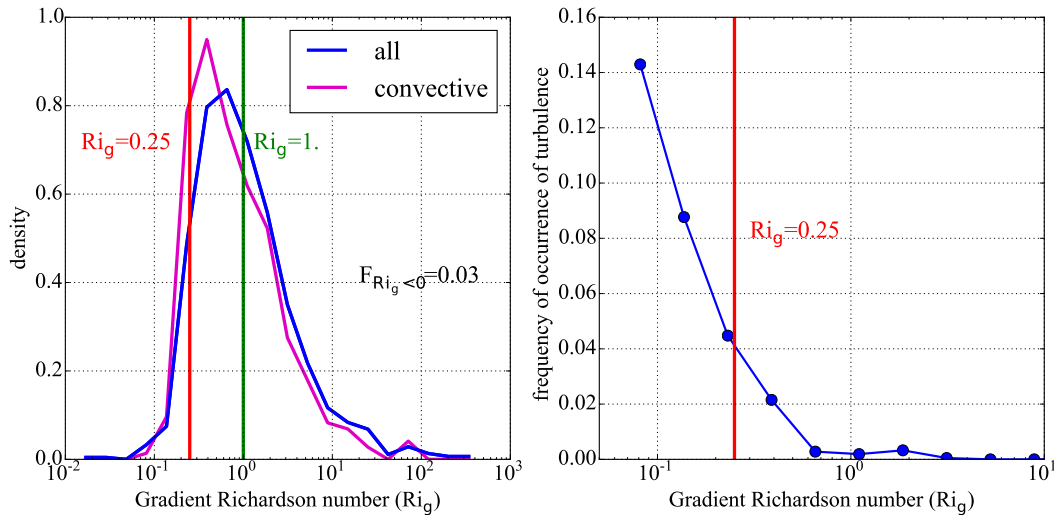


FIG. 8. (left) Empirical distribution of Ri_g from ATTREX descents, calculated over 200-m-deep layers (blue curve). The magenta curve is the same, but for descents less than 100 km from convection. (right) Frequency of occurrence of turbulence as a function of Ri_g .

a. Characterization of an active layer

In Fig. 5, an active and a quiet period are identified in the time series by the yellow and green shadings. Figure 10 shows the cross-wavelet amplitude and phase spectrum between w and θ . The integral across space and wavenumber of its real part corresponds to the heat flux $w'\theta'$. The amplitude spectrum is represented by the colors (log scale) while the arrows correspond to the phase. The active and quiet periods are clearly seen in the increase of amplitude at small scales starting near 300 s. On top of the intermittency of the flux amplitude, the strong time and frequency variability of the phases during the active period can also be noticed, with no obvious polarization relation. This is in striking contrast with the polarized low-frequency signature of the gravity wave centered at 200 s and frequency $10^{-1.5}$ Hz, which indicates phase quadrature between temperature and vertical wind, as expected for a monochromatic gravity wave. Conversely, the absence of well-defined polarization relations at the high frequencies near 400 s supports the idea of “turbulent inertia” dominating at those scales (below 200 m or for wavenumbers larger than $5 \times 10^{-3} \text{ m}^{-1}$).

Figure 11 shows the power spectral density of vertical, horizontal transverse and longitudinal velocity, and of potential energy $E_p(k)$ as a function of horizontal (linear) wavenumber $k = \kappa/2\pi$ (where κ is the angular wavenumber in radians per meter) during the active and quiet time sections. The power spectra $F(k)$ are defined such that $\int_0^\infty F(k)dk = \sigma_{\text{rms}}^2$ where σ_{rms} is the root-mean-square of the variable. The potential

energy spectra is calculated from the potential temperature spectra as

$$E_p(k) = \frac{1}{2} \frac{g^2}{N^2} \frac{\theta^2(k)}{\theta^2}, \quad (8)$$

where $N = g\bar{T}(d\bar{T}/dz + g/C_p)$ is estimated using the vertical temperature gradient inferred from the microwave temperature profiler (MTP; Mahoney and Denning 2009) and averaged over the time section.

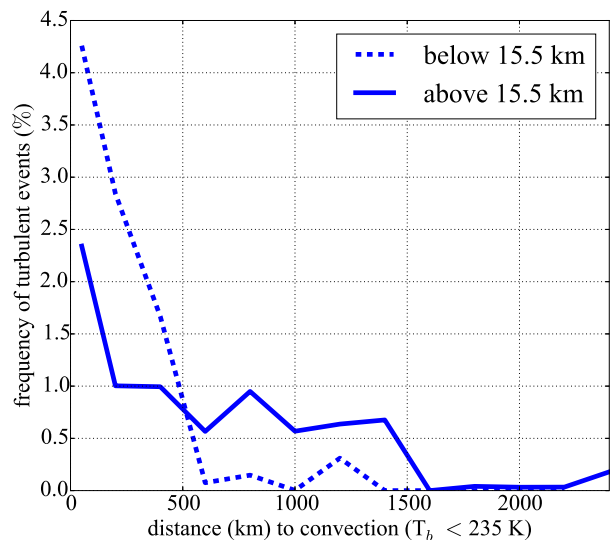


FIG. 9. Occurrence frequency of turbulent bursts vs distance to convection, defined as regions with $T_b < 235$ K. The brightness temperature T_b is that of the $10.8\text{-}\mu\text{m}$ -window channel of the corresponding geostationary satellite (MTSAT or GOES-West).

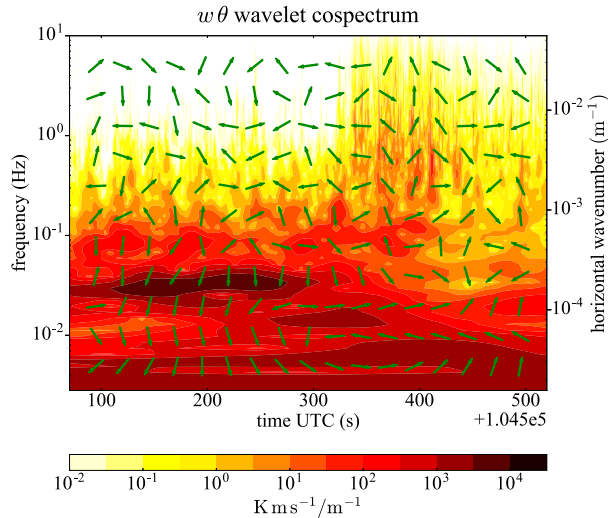


FIG. 10. Cross-wavelet amplitude (colors) and phase (arrows) spectrum of vertical wind w and potential temperature θ . Horizontal arrows directing toward the right (left) indicate that the two fields are in phase (out of phase), while the vertical arrows correspond to fields in quadrature.

During the active period, both transverse velocities (vertical w and horizontal u_t) show a slope from -1.5 to -1.6 , close to the expected $-5/3 \approx -1.66$ for inertial-range turbulence. Similarly, the second-order structure function has a $\sim 2/3$ slope (not shown). The longitudinal, along-track velocity spectrum drops quickly for scales below 500 m, which is a retrieval artifact as explained in section 2. Nevertheless, transverse wind speed w and u_t are at similar activity levels, which again suggests nearly isotropic turbulence. The eddy dissipation rates inferred from vertical and horizontal wind speed only are also shown in Fig. 5; they are of close amplitude and also suggest nearly isotropic turbulence.

These observations (isotropy of winds and $-5/3$ slope) strongly suggest that we are observing inertial-range turbulence. Indeed, during the active period, $\varepsilon_k \approx 10^{-3} \text{ m}^2 \text{ s}^{-3}$ (Fig. 5) and $N \approx 10^{-2} \text{ rad s}^{-1}$ so that the outer scale $L_m \approx 300 \text{ m}$ (wavenumber $1/L_m \approx 3 \times 10^{-3} \text{ m}^{-1}$), which is roughly consistent with the scale at which the $-5/3$ slope starts in Fig. 11.

Regarding the potential energy (per unit mass) power spectral density, Fig. 11 shows that it exhibits somewhat different features than the velocities. Its magnitude is about 10 times smaller than that of u_t ; this disagrees with an interpretation in terms of mid-frequency internal gravity waves for which there is an equipartition expected and observed between potential and total kinetic energy (see, e.g., Fig. 1 of Podglajen et al. 2016a). However, an excess of turbulent kinetic energy compared to turbulent potential energy has been reported in the literature for inertial

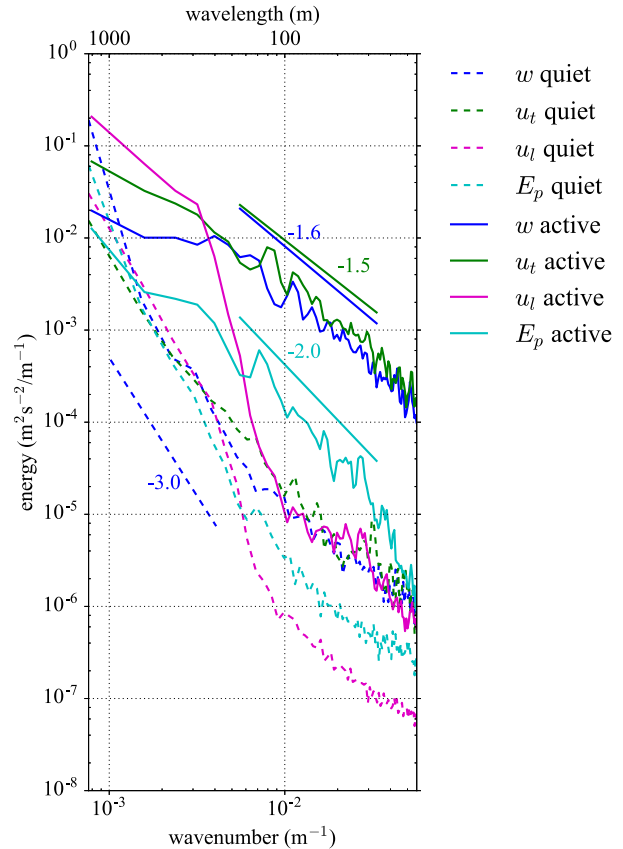


FIG. 11. Power spectral densities of measured winds and potential energy (deduced from temperature and N^2) during a turbulent burst and a quiet period on 16 Feb 2014 near Guam shown in Fig. 5.

turbulence at the finest scales (Wilson et al. 2014). In the figure, the slope of the potential energy spectrum with respect to horizontal wavenumber appears steeper than that of the wind spectra and the $-5/3$ slope expected from theory. The steeper slope observed for E_p probably comes from the response time of the temperature sensor, as explained in section 2.

The turbulence scaling and the statistics of energetics during all ATTREX turbulent bursts are now explored more systematically in the whole dataset in the following subsections.

b. Scaling of wind and temperature during turbulent bursts

The Kolmogorov $k^{-5/3}$ spectra of winds are an important prediction of inertial-range turbulence theory. The power-law scaling slope s —that is, the slope of the log-log linear energy spectrum: $E(k) \propto k^{-s}$ —is expected to be close to $-5/3 \approx -1.66$. At larger scales, we note that theories suggesting different slopes exist: for instance, Lumley (1964) predicts a k^{-3} buoyant subrange,

and indeed there have been observations in the 200–20 km range of steeper slopes than $-5/3$, from -2.5 to -3 (e.g., Nastrom et al. 1987; Chan et al. 1998). In Fig. 11, a steep slope (about -3) is observed for the quiet case at scales of 100 m–1 km.

Figure 12 shows the PDF of s observed during turbulent events. The slopes are computed from the logarithm of the ratio of wavelet power at scales of 0.5 s (90 m) and 0.1 s (18 m). While there is some variability, the $-5/3$ scaling is statistically well verified for transverse horizontal wind u_t . The vertical wind shows slightly shallower slope (-1.54), which is due to the 90-m scale being sometimes higher than the outer scale of the inertial range L_m , so that some of the flat low-frequency part of the w spectrum is included in the slope calculation. Nevertheless, the difference is small, and Fig. 12 shows that a statistical $-5/3$ is verified for vertical and transverse wind. Some variability in the slope exists but a significant part of it can be attributed to sampling uncertainty.

c. Isotropy of small-scale motions

Figure 13 presents the distribution of the ratio between small-scale horizontal and vertical kinetic energy $\sigma_{u_t}^2/\sigma_w^2$ during turbulent bursts. Turbulent bursts are selected depending on the kinetic energy dissipation rate being over the chosen threshold for turbulence $\varepsilon_{\text{lim}} = 10^{-3} \text{ m}^2 \text{ s}^{-3}$. For those events, the motions appear statistically close to isotropy with nevertheless higher variance in the horizontal motions; this is related to our choice of ε_{lim} . Indeed, choosing $\varepsilon_{\text{lim}} = 10^{-3} \text{ m}^2 \text{ s}^{-3}$ generally places the outer scale L_m between 120 and 300 m—that is, near the upper limit of the ~ 18 –90-m range used to estimate small-scale variance so that the motions are close to but not perfectly isotropic. Choosing a higher (lower) threshold to select turbulent bursts increases (decreases) their isotropy (not shown), in agreement with Wroblewski et al. (2010), who also found more isotropy associated with stronger turbulence in aircraft observations in the Southern Hemisphere midlatitude UTLS. It should be noted that the sampling of high ε_k is necessary to obtain nearly statistical isotropy at our observing scales: for instance, Schumann et al. (1995) obtained strong anisotropy ($\sigma_{u_t}^2/\sigma_w^2 \simeq 10$) but sampled much quieter air ($\varepsilon_k \leq 10^{-7} \text{ m}^2 \text{ s}^{-3}$).

If the motions appear almost isotropic on average in Fig. 13, there is a significant dispersion of the $\sigma_{u_t}^2/\sigma_w^2$ ratio from case to case. Direct numerical simulations (e.g., Fritts et al. 2009) and experiments (e.g., Sreenivasan 1991) have reported significant anisotropy of turbulence arising in sheared and stratified flows. The numerous vertical profiles through the TTL acquired during the campaign allowed the sampling of a variety of

stratifications, which is important for the outer scale [Eq. (6)], so that the impact of this parameter can be tested. Figure 13 shows the distribution of $\sigma_{u_t}^2/\sigma_w^2$ for high and low stability N^2 ($N^2 > 4 \times 10^{-4} \text{ s}^{-2}$ and $N^2 < 10^{-4} \text{ s}^{-2}$). Higher N^2 are associated with a higher variance of the horizontal motions relative to vertical ones. This is intuitive: since the atmosphere is then more stratified, vertical motions are inhibited compared with horizontal ones. Furthermore, since the threshold for burst selection ε_{lim} is the same for the different values of N^2 , the high N^2 values correspond to smaller Ozmidov and outer scales. Thus, there is more contribution from anisotropic motions in the 18–90-m range. Consistently, taking the integration over larger scales (40–200 m) to estimate the variance statistically shows more anisotropic motions—that is, a more important contribution of the horizontal motions compared with vertical ones (not shown).

d. Variability in small-scale activity

Figures 5 and 6 show that there is an order of magnitude variability in the estimated ε_k . Turbulent events occur as a succession of bursts, and the observed distribution of ε_k approximately follows a lognormal distribution (Fig. 6), as would be expected from Kolmogorov's third hypothesis and is generally found in observational estimates of dissipation rates (e.g., Wilson 2004; Sharman et al. 2014). Thus, the mean ε_k is dominated by rare, localized, intense events. This characteristic of turbulent bursts, sometimes referred to as intermittency, has important consequences for the effect on turbulent mixing and should be quantified. Previous works have devoted much attention to the characterization of intermittency and multifractal properties of atmospheric turbulence (e.g., Schmitt et al. 1994; Lovejoy and Schertzer 2011). Here, we provide simple quantification of this intermittency using the Gini coefficient (Gini 1921).

Designed to diagnose inequalities of income, the Gini coefficient has been previously used in atmospheric sciences to quantify variability in the momentum flux carried by gravity waves to the stratosphere (Plougonven et al. 2013). It is expressed as

$$G_{\varepsilon_k} = \frac{\sum_{m=1}^M \left[m \bar{\varepsilon}_k - \sum_{i=1}^m (\varepsilon_k)_i \right]}{\sum_{m=1}^M m \bar{\varepsilon}_k}, \quad (9)$$

where $(\varepsilon_k)_m$ is the m th sample from the series of ε_k measurements sorted in increasing order, M is the number of samples, and $\bar{\varepsilon}_k = (1/M) \sum_{m=1}^M (\varepsilon_k)_m$ is the average eddy dissipation rate. The term G_{ε_k} quantifies

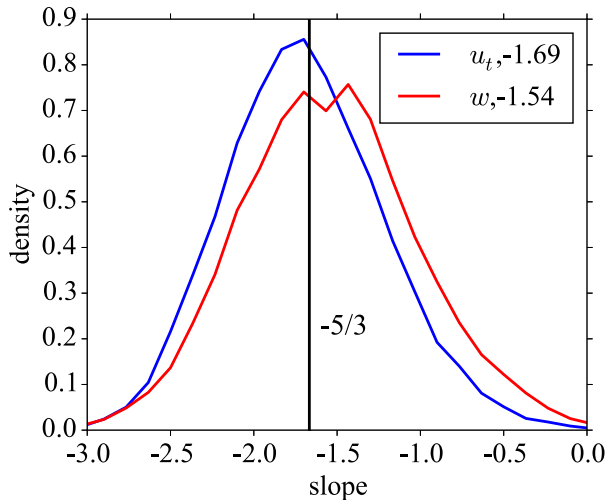


FIG. 12. PDF of spectral slopes of transverse horizontal wind u_t and vertical wind w during the turbulence bursts ($\varepsilon_k > \varepsilon_{\text{lim}}$) for frequencies between 2 and 10 Hz. It is usually close to $-5/3$.

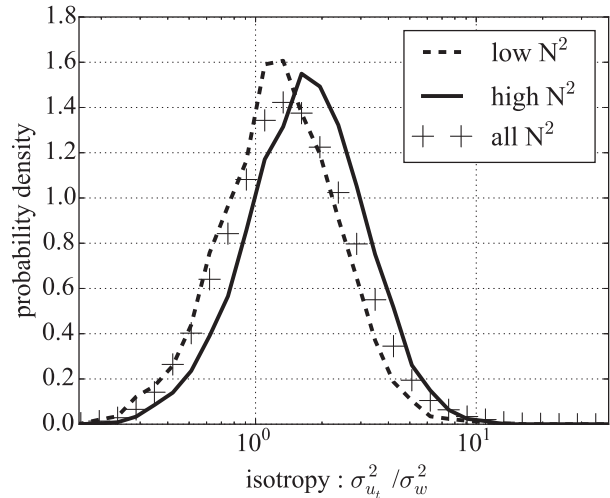


FIG. 13. Ratio of horizontal to vertical kinetic energy $\sigma_{u_t}^2/\sigma_w^2$ (black) for high ($N^2 > 4 \times 10^{-4} \text{ s}^{-1}$; dashed), low ($N^2 < 10^{-4} \text{ s}^{-1}$; solid), and all (crosses) stability.

statistical dispersion in the eddy dissipation rate—that is, the relative importance of the tail of the PDF of ε_k on its integrated value. A $G_{\varepsilon_k} = 0$ corresponds to a constant ε_k for which all measurements equally contribute to the sum. A $G_{\varepsilon_k} \rightarrow 1$ corresponds to a highly inhomogeneous turbulent field: a single measurement accounts for the total sum [all $(\varepsilon_k)_m = 0$, except $(\varepsilon_k)_M > 0$]. For intermediate values, the exponential distribution for instance has $G_{\varepsilon_k} = 0.5$. The Gini coefficient thus provides a quantitative measure of the relative contribution of the upper part of the tail to the average value.

The empirical G_{ε_k} values obtained for different regions and altitude ranges are summarized in Table 1. Contrary to regional averages $\bar{\varepsilon}_k$, all values of the Gini coefficient are fairly similar and extremely high (close to 0.95), which emphasizes the dominant contribution of a few rare events to the average ε_k . For comparison purposes, the highest typical Gini coefficients for income are lower than 0.7; gravity wave momentum flux in the lower stratosphere also have Gini coefficients lower than 0.7 (e.g., Plougonven et al. 2013). Eddy dissipation rates in the TTL are therefore highly inhomogeneous.

e. Size of active turbulent patches

Being intermittent, small-scale activity is localized in patches of limited size. This locality of turbulence is important to assess the level of the vertical eddy diffusion induced by turbulent patches (Dewan 1981; Alisse and Sidi 2000; Vanneste 2004; Osman et al. 2016).

Aircraft descents are used in order to infer the depth of the observed layers, a turbulent layer being defined as a continuous segment of $\varepsilon_k \geq 10^{-5} \text{ m}^2 \text{ s}^{-3}$ containing at least one occurrence of $\varepsilon_k \geq \varepsilon_{\text{lim}} = 10^{-3} \text{ m}^2 \text{ s}^{-3}$. As

previously mentioned, there is a crude approximation in considering aircraft descents as strictly vertical profiles, given the huge horizontal speed of the plane compared to the vertical descent rate. This approximation is partly justified by the aspect ratio of the atmospheric flow in the TTL and its impact on the structure of turbulent layers, which are vertically thin and extend horizontally. The distribution of layer depths inferred from the 136 aircraft descents is presented in Fig. 14. The selected descents are more than 2 km deep and generally 3–4 km deep (from 14 to 18 km), which limits the upper detectable depth of the encountered layers. However, Fig. 14 shows that the layers are found less than 500 m deep, and most of them have depth on the order a few 100 m or less. Furthermore, most observations of turbulence (95%) and of turbulent layers (93%) are within a layer with an identified top and bottom. On the other hand, very few occurrences of layers narrower than a few tens of meters are found. This is probably due to the limit imposed by the minimum detectable depth with our measurements in the 20–90-m range, since the outer scale of turbulence L_m should be no larger than the depth of the turbulent patches and we are limited to $L_m > \sim 20\text{--}100 \text{ m}$. Finding typical turbulent layers from a few tens to a few hundred meters deep is roughly consistent with findings from radiosondes (Wilson et al. 2011).

Figure 14 also shows the distribution of the patches' horizontal sizes, inferred from continuous straight horizontal aircraft segments. Typical patches are from a few tens to hundreds of kilometers long, but the sampling of this distribution might be limited by the limited resolution and the typical size of straight segments during ATTREX (less than 200 km). Indeed, a little more than

TABLE 1. Mean ε_k and Gini coefficient of ε_k in different regions and altitude range: all ATTREX flights, eastern or western Pacific flights only, and upper (above 15.5 km) and lower (below 15.5 km) TTL.

	All ATTREX	Eastern Pacific	Western Pacific	Upper TTL	Lower TTL
$\overline{\varepsilon_k}$ ($10^{-5} \text{ m}^2 \text{ s}^{-3}$)	5.6	3.4	8.2	4.3	9.7
G_{ε_k}	0.96	0.96	0.95	0.96	0.95

20% of turbulent observations during those straight segments have their bounds outside of the sampled segment, so that the actual size of the associated turbulent patch cannot be determined. We also note that if turbulent patches are slightly tilted, the horizontal size will be underestimated. Hence, Fig. 14 only provides a lower estimate of horizontal sizes.

Finally, we note that the typical horizontal and vertical sizes might seem lower than those estimated by Sharman et al. (2014): this is probably mainly due to the fact that those authors quantified turbulence using thresholds on the peak EDR ($\varepsilon_k^{1/3}$) within 1 min, instead of instantaneous EDR value as in our study.

6. Estimation of the impact on vertical mixing

Turbulence active patches have long been reckoned to control the vertical diffusion of constituents in the UTLS (Dewan 1981; Mote et al. 1996), and this effect is

usually represented by a turbulent diffusivity. However, the value of the effective diffusivity resulting from the activity of all patches remains a matter of debate. Assuming perfect mixing inside the turbulent patches and no mixing out of them, Dewan (1981) deduced a typical mean diffusivity on the order of $0.2 \text{ m}^2 \text{ s}^{-1}$. This value is at odds with estimates derived from observed tracer evolution and structure: using the water vapor tape recorder in the tropical lower stratosphere, Mote et al. (1998) concluded that the typical value in that region should rather be on the order of $0.02\text{--}0.03 \text{ m}^2 \text{ s}^{-1}$. Generally, available estimates vary by a few orders of magnitude (from 0.01 to $1 \text{ m}^2 \text{ s}^{-1}$; Mote et al. 1998; Legras et al. 2003; Rao et al. 2001; Sunilkumar et al. 2015; Glanville and Birner 2017). Although particularly strong in the TTL, uncertainties in the magnitude of turbulent diffusivity are also found in other regions of the atmosphere [see Table 1 of Wilson (2004) for a review of diffusivity estimates in different regions].

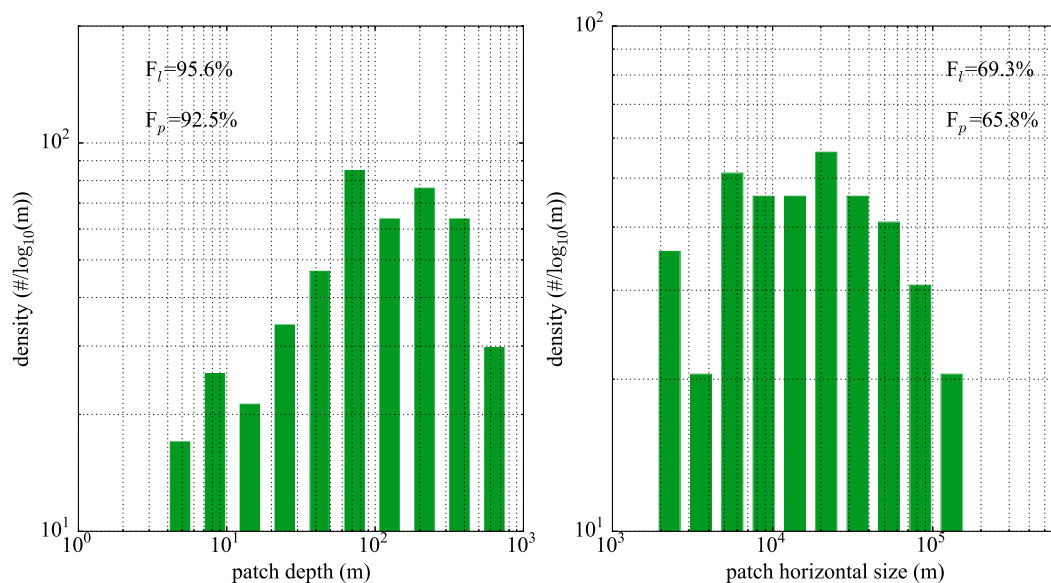


FIG. 14. Distribution (number of occurrence normalized by bin size) of (left) turbulent patches depth and (right) horizontal size. These are obtained from vertical descents of the aircraft and from straight horizontal scans, respectively, and patches are defined as continuous segments with $\varepsilon_k \geq 10^{-5} \text{ m}^2 \text{ s}^{-3}$ and at least one occurrence of $\varepsilon_k > \varepsilon_{\text{lim}} = 10^{-3} \text{ m}^2 \text{ s}^{-3}$. The proportion of sampled patches F_l and of sampled turbulent points F_p entering in the statistics are indicated; they do not reach 100% because the bounds of the patches sometimes occur outside of the scans. The values of F_u and F_p thus indicate the reliability of the presented size statistics.

a. *Estimation of turbulent diffusivity from aircraft observations*

The turbulent diffusion coefficient for heat is defined as

$$K_h = -\frac{\overline{w'\theta'}}{\frac{d\theta}{dz}}. \quad (10)$$

It is related to the turbulent diffusivity K_χ of the tracer of mixing ratio χ , through the turbulent Lewis number L_e :

$$K_\chi = -\frac{\overline{w'\chi'}}{\frac{d\chi}{dz}} = L_e K_h, \quad (11)$$

where L_e is generally assumed to be close to 1 in the free atmosphere, so that the heat diffusivity is the same as the diffusivity for tracer transport $K_\chi = K_h$.

Assuming spatial homogeneity and stationarity of the turbulence (for lack of a better alternative), K_h can be related to the potential energy dissipation rate (see, e.g., Lilly et al. 1974; Wilson 2004), following

$$K_h = \frac{\varepsilon_p}{N^2}. \quad (12)$$

It is also related to the kinetic energy dissipation rate:

$$K_h = \gamma \frac{\varepsilon_k}{N^2}, \quad (13)$$

where $\gamma = \varepsilon_p/\varepsilon_k$ is the dissipation rate ratio (Wilson 2004). Under the hypotheses of homogeneity and stationarity, $\gamma = R_f/(1 - R_f)$, where R_f is the flux Richardson number. Lilly et al. (1974) suggest a canonical value of $R_f = 0.25$, based on Thorpe (1973), corresponding to $\gamma = 1/3$. Weinstock (1978a) argues for $\gamma \simeq 0.8$. Radar observations by Dole et al. (2001) actually show γ to be highly variable and dependent on the stability and on the life cycle of the turbulent patch. A typical value of γ from their study is 0.2—not so different from 1/3.

One method for estimating K_h consists in applying Eq. (13) using the estimated ε_k and the vertical stability from the microwave temperature profiler (Mahoney and Denning 2009) temperature lapse rate. It has been used by Lilly et al. (1974) and Schumann et al. (1995). The main uncertainty for this method comes from the poorly constrained parameter γ , which, as just discussed, probably depends on various parameters (e.g., the stage of evolution of the turbulent layer).

Another method would consist in directly using the time series of w and θ to evaluate the flux $w'\theta'$ from the covariance between w and θ using some spatial average and deduce the diffusivity using the vertical temperature

gradient (Kennedy and Shapiro 1975, 1980; Pavelin et al. 2002). Apparently more direct, this method requires assuming 1) the scale of the perturbations at which to calculate the flux and 2) the distance over which to average the flux. As $\overline{w'\theta'}$ is strongly intermittent (see Fig. 10), the output of this procedure is dependent on the scales chosen for averaging, which are difficult to physically justify. Tests led to very weak and upgradient potential temperature flux. Furthermore, given the intermittency of turbulence, it is not guaranteed that this approach will provide a reliable estimate of the ensemble average implied in the definition of K_h . For this reason and because of uncertainties in the high-frequency temperature measurements, we use the first method to estimate K_h in the following with Lilly's value for γ ; that is, $\gamma = 1/3$.

b. *Impact on tracer transport: Effective vertical eddy diffusivity*

A natural approach to estimate the average impact of the observed turbulent diffusion is to consider the average diffusivity \overline{K} . However, as recently reviewed by Osman et al. (2016), this might overestimate the effect on tracer transport, which would be inferred from satellite observations of tracers (as in, e.g., Mote et al. 1996). Indeed, turbulence appears within a limited number of shallow patches, and the mixing is confined within those patches. In the extreme case of perfectly mixed but very small patches, the strong mixing within the layer will not overcome the fact that no diffusion takes place out of the very shallow layer; one can thus get a large average diffusivity with virtually no impact on tracers. To estimate the impact of the finite-size turbulent patches on the transport of trace gases, different authors (e.g., Dewan 1981; Alisse et al. 2000; Vanneste 2004; Osman et al. 2016) have introduced an effective diffusivity K_{eff} .

Alisse et al. (2000) and Vanneste (2004) propose the following expression for the effective diffusivity:

$$K_{\text{eff}} = F_t \frac{\overline{h_p^3}}{12h_p\tau_p} (1 - c), \quad (14)$$

$$c = \frac{96}{\pi^4 \overline{h_p^3}} \sum_{n=0}^{\infty} \frac{h_p^3 \exp[-(2n+1)^2 \delta_p]}{(2n+1)^4},$$

where F_t is the so-called turbulent fraction, h_p is the depth of turbulent patch p , τ_p its lifetime, $\overline{(\dots)}$ is the ensemble average, and $\delta_p = \pi^2 K_p \tau_p / h_p^2$ quantifies the intensity of mixing within the patches, with K_p the turbulent diffusivity within the patch. The parameter c is bounded ($0 \leq c \leq 1$) and quantifies the impact of

small-scale mixing within the patches: $c = 0$ ($\delta_p \rightarrow \infty$) corresponds to the perfect mixing, while if $c = 1$ ($\delta_p = 0$), there is virtually no mixing. In the imperfect mixing limit ($\delta_p \ll 1$), Vanneste (2004) has shown that this expression can be simplified in

$$K_{\text{eff}} = F_t \frac{\overline{h_p K_p \tau_p}}{\overline{h_p \tau_p}}. \quad (15)$$

In that case, one recovers $K_{\text{eff}} = \overline{K}$; that is, the ensemble average of the turbulent diffusivity [computed, e.g., from Eq. (13)] is also the effective diffusivity seen by mean tracer transport. It can be noted that both Eqs. (14) and (15) emphasize the prominent contribution of the deepest patches to the resulting effective diffusivity K_{eff} , which suggests that the vertical resolution of ATTREX observations is sufficient for vertical mixing estimates.

Equation (14) suggests that an upper bound on effective diffusivity may be written as $K_{\text{eff}}^{\text{full}} = F_t (\overline{h_p^3} / 12 \overline{h_p \tau_p})$. It is independent of turbulence strength within the patches and corresponds to the fully mixed regime [as used by Dewar (1981)]. Using the layer depth distribution derived in the previous section, and assuming a typical layer lifetime τ_p of 1 h, as suggested by numerical simulations of turbulence (Fritts et al. 2009) and radar observations (Wilson et al. 2005), we find $K_{\text{eff}}^{\text{full}} \simeq 0.18 \text{ m}^2 \text{ s}^{-1}$. The estimated value of $K_{\text{eff}} \simeq 0.04 \text{ m}^2 \text{ s}^{-1}$ is a factor of ~ 4 lower than the full mixing estimate, so that the assumption of perfect tracer mixing within turbulent layers is probably not suitable for the TTL. The ensemble average estimate $\overline{K} \simeq 0.06 \text{ m}^2 \text{ s}^{-1}$ still overestimates K_{eff} , but by no more than 50% (we note, however, that this will depend on the assumed lifetime τ_p). We therefore regard \overline{K} as a reasonable practical approximation to K_{eff} since the resolution of aircraft observations gives access to the deepest, most active layers. Furthermore, the observations show that tracer variance is enhanced within turbulent patches, arguing against complete mixing (not shown). Finally, this estimate is natural and has practical advantages: it can be computed with better sampling since all data can be used, it is not restricted to aircraft descents nor does it require assumptions on the patch lifetime and turbulence structure. We therefore use this mean diffusivity in the following and work in the imperfect mixing limit of Vanneste (2004).

c. Turbulent diffusivity in the tropical tropopause layer and comparison with ERA-Interim and other observations

Figure 15 shows the average profile of turbulent diffusivity inferred from all ATTREX flights. The estimated values decrease from the bottom to the top of the

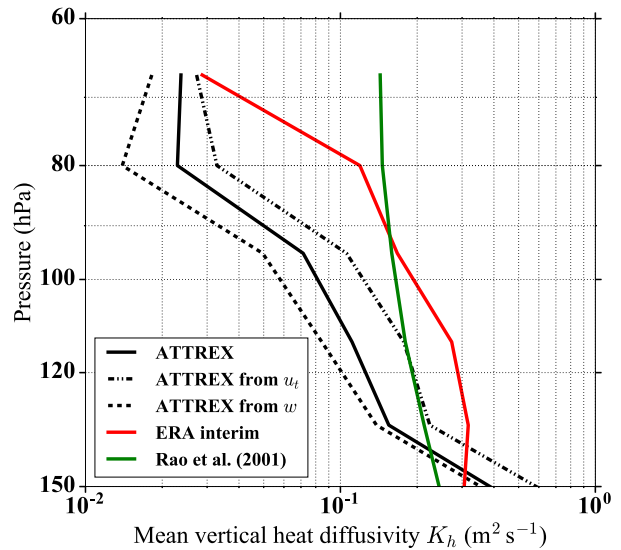


FIG. 15. Average vertical profile of turbulent diffusivity inferred from ATTREX observations using $K_h = (1/3)(\epsilon_k/N^2)$ and from ERA-Interim along the aircraft trajectory. The ERA-Interim profile is not very different from the mean profile over the tropical Pacific, showing the reasonable sampling obtained with the aircraft.

TTL, consistent with the altitude distribution of turbulent events (Fig. 7). Typical values are between 0.02 and $0.1 \text{ m}^2 \text{ s}^{-1}$. For comparison purposes, we consider here the average of all vertical diffusivity estimates within a fixed layer (about 1 km deep).

Figure 15 exhibits a strong decrease of turbulent diffusivity with increasing altitude. We note that this is in a small part biased by the fact that both 2014 and 2013 statistics are merged in this figure and that 2014 was both more turbulent and had more flight segments in the lower TTL so that the increase at the lowest levels is mainly a 2014 feature (see also Fig. 7). However, this increase is also seen in the eastern Pacific (though less strongly) because the computation of turbulent diffusivity involves the inverse of the stability [Eq. (13)], which decreases rapidly with altitude in both the eastern and western Pacific TTLs.

In Fig. 15, the estimated vertical profile is compared with the turbulent diffusion from ERA-Interim (ECMWF 2009) interpolated along the flight tracks. While the strong decrease of diffusivity with altitude is a common feature of the observations and the analysis, the discrepancy in magnitude is as much as a factor of 3. We emphasize that our estimate might be biased owing to the uncertainties in the retrieved ϵ_k and to the ad hoc parameter γ ; however, for the latter, the observations of Dole et al. (2001) would rather suggest that we overestimate it. The amplitude of this discrepancy is then significant. Still, it should be noted that order of magnitude differences in the average vertical diffusivity are

commonly observed between models. For instance, in the general circulation model CAM, Bardeen et al. (2013) showed that the change of the PBL scheme (which is applied over the whole atmosphere for the parameterization of turbulent processes) between CAM4 and CAM5 resulted in a more than two orders of magnitude change in the vertical diffusivity. This caused major issues for the water vapor budget of the tropical UTLS, and the diffusivity had to be artificially reduced to avoid an unrealistically wet lower stratosphere. Thus, it may not be possible to attribute with certainty the discrepancy of our estimate with ERA-Interim either to model or observational deficiencies. However, we note that, using a completely different approach based on the water vapor tape recorder signal in the lower stratosphere, Glanville and Birner (2017) also suggested an overestimated vertical diffusivity in ERA-Interim, with a tape recorder water vapor signal ascending faster and being attenuated more rapidly than in satellite observations.

Comparing with other observational estimates, we note that ATTREX values are also generally below typical estimates from radar observations over Japan or India. Using mid- and upper-atmosphere (MU) radar measurements, Fukao et al. (1994) over Japan and Rao et al. (2001) over Gadanki (India) report median vertical diffusivity values on the order of 10^{-1} – 10^0 and 10^{-1} – $3 \times 10^{-1} \text{ m}^2 \text{ s}^{-1}$, respectively, in our altitude range. The typical median data reported by Rao et al. (2001) for the year 1995/96 are also represented in Fig. 15, showing that they exceed our estimates by a factor of 6 at the upper levels while being in closer agreement at lower levels. The values reported by Rao et al. (2001) do not exhibit as strong an altitude dependence. While the fact that those authors represent the median (rather than the mean) value of their estimated K_h might bias the comparison, this is clearly not sufficient to explain the discrepancy, which is a factor of 5–6 in the upper TTL. Rao et al. (2001) emphasized more active turbulence during the monsoon period (a factor of 2 or more) and diffusivity a factor 2 times smaller in the ENSO year 1998, so that part of the observed difference might rather come from this seasonal, interannual, and geographical variability. Generally, our values are well below those reported by Fukao et al. (1994) but closer and compatible with those reported by Rao et al. (2001).

Alappattu and Kunhikrishnan (2010) estimated vertical diffusivity from high-resolution radiosonde observations over the Bay of Bengal and the Arabian Sea and also found a decrease of about one order of magnitude from the bottom to the top of the TTL. However, they obtained values about one order of magnitude higher than those estimated from ATTREX (from a few

10^{-1} to about $10^1 \text{ m}^2 \text{ s}^{-1}$). Using similar observations, Sunilkumar et al. (2015) evaluated vertical diffusivity over Gadanki and Trivandrum, India, and found values about two orders of magnitude higher than those found in our study (from 10^0 to $10^1 \text{ m}^2 \text{ s}^{-1}$). The decrease of K_h by one order of magnitude from the bottom to the top of the TTL is also found in their study, but there is no agreement on the magnitude. The different regions and periods are probably insufficient to explain the discrepancy of ATTREX values with those studies. However, Sunilkumar et al. (2015) noted that the values obtained in their study were much higher than obtained in other works, which might come from the uncertainties in some poorly known coefficients used in estimating K_h from radiosondes.

d. Impact on some TTL tracers: O_3 , CO , and H_2O

The impact of small-scale turbulent diffusivity on vertical tracer transport in the TTL and lower stratosphere can be compared with the impact of the mean vertical transport by tropical upwelling. It should be noted, however, that small-scale turbulent diffusivity is also important in controlling the exchange with the extratropics, by diluting the large-scale extratropical intrusions that arise as a result of breaking Rossby waves. For the purpose of comparing turbulent diffusivity with vertical advection by tropical upwelling, we derive an equivalent vertical speed for different tracers. The turbulent vertical flux of the tracer χ is

$$\overline{w'\chi'} = -K_h \frac{\partial \bar{\chi}}{\partial z} = \bar{w}_{\chi_{\text{eq}}} \bar{\chi}. \quad (16)$$

The equivalent vertical speed is $\bar{w}_{\chi_{\text{eq}}} = -K_h(\partial \bar{\chi}/\partial z)(\bar{\chi})^{-1} = K_h/D_\chi$, where

$$D_\chi(z) = -\frac{1}{\frac{d \ln(\bar{\chi})}{dz}} \quad (17)$$

is the length of exponential decay (increase) with altitude z of the tracer mixing ratio.

The exponential lengths $D_\chi(z)$ are estimated from multiyear tropical mean profiles derived from the *Aura* Microwave Limb Sounder, published in Randel et al. (2007) for O_3 and CO and Fueglistaler et al. (2009) for H_2O . They are given in Table 2, together with the typical equivalent vertical speed in the upper and lower TTL obtained from our estimate of turbulent diffusivity. In the upper TTL and lower stratosphere, the equivalent vertical speed associated with turbulent diffusivity is generally one order of magnitude lower than the mean upwelling speed (typically $2 \times 10^{-4} \text{ m s}^{-1}$ in the upper TTL). This agrees with previous studies that showed

TABLE 2. Exponential length D_χ and equivalent vertical speed $w_{\chi_{\text{eq}}}$ induced by vertical eddy mixing due to tracer transport, in the upper TTL (near 80–90 hPa) and in the lower TTL (near 150 hPa). Those should be compared to the dynamical upwelling speed, which is about $2 \times 10^{-4} \text{ m s}^{-1}$ at 80 hPa.

	Tracer	O ₃	CO	H ₂ O
Upper TTL	D_χ (km)	−1.25	3.4	3.8
	$w_{\chi_{\text{eq}}}$ (10^{-4} m s^{-1})	−0.16	0.06	0.05
Lower TTL	D_χ (km)	−10	15	1.1
	$w_{\chi_{\text{eq}}}$ (10^{-4} m s^{-1})	−0.40	0.27	3.6

that for those tracers the variability was dominated by the variability in mean tropical upwelling (e.g., Randel et al. 2007; Abalos et al. 2013). Ozone is the examined constituent for which the estimated $\bar{w}_{\chi_{\text{eq}}}$ is the strongest in the upper TTL, but it is less than 10% of the annual mean upwelling (which is itself lower than the winter value when the annual cycle peaks). In the lower TTL, the equivalent speeds are higher owing to higher diffusion, especially for species with strong vertical gradients such as water vapor; however, at these altitudes, direct convective injection, mixing between convective overshoots and their environment, and higher mean upwelling (Randel et al. 2008) probably dominate the vertical transport. The impact of vertical diffusion on vertical transport may be larger for other short-lived tropospheric species that have stronger gradients in the lower TTL. However, these calculations suggest that the major role of turbulent diffusion is probably not as much in its impact on vertical transport as in the mixing impact, such as the dilution of the tape recorder signal in water vapor or in the mixing of intrusions from the midlatitudes.

7. Summary and conclusions

This paper characterized the occurrence of small-scale (18–90 m) wind and temperature fluctuations in the tropical tropopause layer over the tropical Pacific from aircraft observations. The fluctuations are found more frequently at the bottom of the TTL and in the western Pacific. They are correlated with shear and low static stability, as quantified by the gradient Richardson number. Since they modify the background wind shear and stability, both inertia–gravity and small-scale gravity waves play a role in turbulence occurrence, as illustrated in a case study. Furthermore, closeness to deep convective clouds, which might generate convective gravity waves, was found to be favorable for the occurrence of turbulence.

During bursts of small-scale activity, the observed fluctuations appear consistent with “inertial range” turbulence à la Kolmogorov. They typically exhibit a $-5/3$ spectrum for the winds and show approximate

isotropy between horizontal and vertical directions. An important property of turbulence in the tropical UTLS is its intermittency: a few rare bursts dominate the variance at small scales, as quantified by the typical value of the Gini coefficient (0.95). Strong turbulence is confined within patches from a few tens to hundreds of meters vertically and a few tens of kilometers horizontally.

Using the approach of Lilly et al. (1974), we used the measured eddy dissipation rate to estimate the diffusivity K_h induced by those turbulent encounters. The average value of K_h in the TTL is typically on the order of $0.1 \text{ m}^2 \text{ s}^{-1}$ but shows a strong gradient (one order of magnitude) from the bottom (a few $0.1 \text{ m}^2 \text{ s}^{-1}$) to the top of the TTL (a few $0.01 \text{ m}^2 \text{ s}^{-1}$). Interestingly, those values are compatible, within a factor of 3–4, with the average diffusivity parameterized in ERA-Interim. This result has important implications for numerical models. Although these models typically do not capture small-horizontal scale and fine vertical-scale waves, the formulation used could be adapted to better represent the mean effect of turbulent bursts on heat transfer. Despite the relative agreement with ERA-Interim, there is a discrepancy of about an order of magnitude or more between aircraft observations and previous estimates from radar or radiosonde observations, which might come from geographic and seasonal differences, but probably also from some poorly constrained coefficients in K_h estimates.

The observed turbulent diffusion might have a significant impact on vertical tracer transport, depending on the vertical profile of the chemical species considered, but its effect is generally lower than the mean tropical upwelling. In the lower TTL, turbulent diffusion may be of secondary importance when compared with convective detrainment, although some modeling studies suggest that it might control the vertical transport of tracers up to the level of zero radiative heating (LZRH) (Konopka et al. 2007). Furthermore, in both the lower stratosphere and the TTL, turbulent diffusion ultimately controls dilution and mixing with the extratropics. Turbulent diffusion might also prove important to simulating cloud properties; the dilution of newly nucleated ice particles after nucleation contributes to modifying cirrus volume and extent, which, in turn, impacts their dehydration efficiency and greenhouse effect. Given the importance of TTL turbulence and the uncertainty of its parameterization in models, further observations are required to assess its magnitude and its seasonal and geographic dependency.

The statistics on turbulence in the TTL presented in this paper will be of use for modelers. They can serve to assess the diffusion schemes used in global climate

models, which are crucial for an accurate representation of the heat and tracer budgets. Such statistics will also prove useful for Lagrangian models; they provide a way to assess the importance of the parameterized diffusion process, which controls tracer mixing.

Acknowledgments. We thank C. Bardeen, J. Bergman, D. Fritts, B. Legras, and R. Wilson for discussions and three anonymous reviewers for their comments that helped improve the manuscript. Most of this work was carried out during a visit of A. P. to the Atmospheric Chemistry Observation and Modeling (ACOM) Division at the National Center for Atmospheric Research (NCAR). NCAR is operated by the University Corporation for Atmospheric Research, under sponsorship of the National Science Foundation. A. P., R. P., and A. H. acknowledge support from the ANR project StraDyVariUS (Stratospheric Dynamic and Variability, ANR-13-BS06-0011-01).

APPENDIX A

Wavelet Estimate of High-Frequency Variance

For aircraft observations time series of N measurements separated by a sampling time step $\delta t = 0.05$ s, the (redundant) scales of the wavelet analysis s_j are given by

$$s_j = s_0 2^{\delta j}, \quad j = 0, \dots, J, \quad (\text{A1})$$

with $J = \delta j^{-1} \log_2(N\delta t/s_0)$ and $s_0 = 2\delta t$. Here we have chosen $\delta j = 0.2$ and checked the accuracy of the corresponding wavelet reconstruction.

The wavelet used is the Morlet wavelet. Its analytical expression as a function of time t is given by

$$\Psi_M(t) = \pi^{-1/4} (e^{i\omega_0 t} - e^{-\omega_0^2/2}) e^{-t^2/2}, \quad (\text{A2})$$

where we have chosen $\omega_0 = 6$, so that the second term in the parenthesis is about 10^{-8} and can be safely dropped.

Although Morlet wavelets are nonorthogonal, the redundancy of the continuous wavelet transform allows an approximate time–frequency decomposition of the variance associated with the fluctuations. Indeed, the obtained time series of wavelet coefficients at different scales $W_n(s_j) = W(s_j, t_n)$ approximately verify Parseval's identity:

$$\sigma^2 \simeq \frac{\delta j \delta t}{C_\delta N} \sum_{n=0}^{N-1} \sum_{j=0}^J \frac{|W_n(s_j)|^2}{s_j} \quad (\text{A3})$$

(within 1%), where σ^2 is the variance of the time series and $C_\delta = 0.776$ for the Morlet wavelet (Torrence and

Compo 1998). Time series of the high-frequency variance σ_{HF} can also be derived as

$$\sigma_{\text{HF}}^2(t_n) \simeq \frac{\delta j \delta t}{C_\delta} \sum_{j=j_1}^{j_2} \frac{|W_n(s_j)|^2}{s_j}, \quad (\text{A4})$$

where only the time scales between s_{j_1} and s_{j_2} have been selected. Unless stated otherwise, we have used $s_{j_1} = s_0 \simeq 0.1$ s and $s_{j_2} = 0.5$ s for estimating the high-frequency variance.

APPENDIX B

Uncertainty in Eddy Dissipation Rate Estimate

In this appendix we discuss the precision and accuracy of the eddy dissipation rate estimates derived from ATTREX MMS observations. The formulas are taken from Scott et al. (1990).

The vertical wind measured by the aircraft is approximately given by (Scott et al. 1990)

$$w = -V_a \sin(\theta - \alpha) + \dot{Z}, \quad (\text{B1})$$

where V_a is the true airspeed measured with Pitot sondes (around 170–180 m s^{-1} for the Global Hawk), θ is the pitch of the aircraft measured with the inertial system, α is the angle of attack (AOA) measured using the radome differential pressure sensors, and \dot{Z} is the aircraft ascent rate, determined from the GPS and the inertial system. In practice, given the atmospheric variability in vertical wind, the dominant term (generally by one order of magnitude) for measuring w at high frequency is the variation of the AOA α . Because of this one term dominating the others rather than having comparable terms that cancel one another, the measurements are actually the most reliable at those high frequencies. The accuracy in the retrieval of $V_a \alpha$ at high frequency controls the accuracy of ε_w estimated in the 2–10-Hz frequency band. In the following we evaluate the uncertainty in w in that specific frequency range.

The accuracy of vertical velocity measurements is $\delta w/w = (\delta V_a/V_a) + (\delta \alpha/\alpha)$. The value of α is retrieved from the radome system vertical differential pressure sensor ΔP using the relation $\alpha = a\Delta P(q)^{-1}$, where a is the airflow angle sensitivity factor, taken to be $a = 1/0.07854^\circ$, and $q = (1/2)\rho V_a^2$ (hPa) is the compressible dynamic pressure, which is evaluated from the difference between total pressure and static pressure.

Regarding the noise level, pitch and AOA are retrieved with a resolution of 0.01° , so that the quantization noise is $\sigma_\theta \simeq \sigma_\alpha \simeq 0.003^\circ$. In the 2–10-Hz frequency

band, the noise level on the vertical velocity variance is on the order of

$$\sigma_W^2 \simeq \frac{8}{10} V_a^2 (\sigma_\alpha^2 + \sigma_\beta^2) \simeq 1.2 \times 10^{-4} \text{ m}^2 \text{ s}^{-2}. \quad (\text{B2})$$

The corresponding noise level on ε_w is

$$\sigma_{\varepsilon_w} = \left[\frac{\sigma_W^2}{2\alpha_k (\kappa_1^{-2/3} - \kappa_2^{-2/3})} \right]^{3/2} \simeq 1.7 \times 10^{-7} \text{ m}^2 \text{ s}^{-3}. \quad (\text{B3})$$

The transverse wind measured by the aircraft is approximately given by Scott et al. (1990):

$$u_t = V_a \sin(\beta) + \dot{Y}_t, \quad (\text{B4})$$

where β is the yaw angle and \dot{Y}_t is the aircraft ground relative speed in the transverse direction. With the yaw being retrieved similarly to the AOA, the corresponding noise level and accuracy of the transverse horizontal wind are similar to the vertical wind, except that the pitch noise does not intervene. We then have $\sigma_{\varepsilon_{u_t}} \simeq 6 \times 10^{-8} \text{ m}^2 \text{ s}^{-3}$.

Finally, the estimate of the eddy dissipation rate relies on wavelet transforms obtained with a limited sampling. Torrence and Compo (1998) explain how to derive the corresponding uncertainty, and we shall follow their methodology. The high-frequency variance was estimated by averaging over wavelet scales:

$$(\sigma_{\text{est}})^2 \simeq \frac{\delta j \delta t}{C_\delta} \sum_{j=j_1}^{j_2} \frac{|W_n(s_j)|^2}{s_j}. \quad (\text{B5})$$

The confidence interval of the true high-frequency variance σ^2 is then

$$\frac{\nu}{\chi_\nu^2(1-p/2)} \leq \frac{\sigma^2}{\sigma_{\text{est}}^2} \leq \frac{\nu}{\chi_\nu^2(p/2)}, \quad (\text{B6})$$

where χ_ν^2 is the value of the chi-square distribution with ν degrees of freedom. For continuous wavelet transforms, the number of degrees of freedom ν can be modeled as [Torrence and Compo (1998), their Eq. (28)]

$$\nu \simeq \frac{2n_a S_{\text{avg}}}{S_{\text{mid}}} \sqrt{1 + \left(\frac{n_a \delta j}{\delta j_0} \right)^2}, \quad (\text{B7})$$

where $n_a = j_2 - j_1 + 1$ is the number of scales used for averaging, $S_{\text{avg}} = \left[\sum_{j=j_1}^{j_2} (s_j)^{-1} \right]^{-1}$ and $S_{\text{mid}} = s_0 2^{0.5(j_1 + j_2)\delta j}$, and $\delta j_0 = 0.6$ for the Morlet wavelet. For ATTREX MMS data, we have used $\delta j = 0.2$ and $n_a = 12$ so that $\nu \simeq 7.4$. The 50% confidence interval for the variance is

then [0.77, 1.61], so that the sampling uncertainty is about 50% for the variance and less than 80% on the eddy dissipation rate for one wind component ε_w or ε_{u_t} . For the geometric mean $\varepsilon_k = \sqrt{\varepsilon_w \varepsilon_{u_t}}$ used in the paper, the uncertainty in instantaneous ε_k is 50% and is reduced to below 25% with 1-s averaging.

The estimate of ε_k is provided at 20 Hz—the frequency of wind observations; however, the wavelet coefficients have an autocorrelation of time of $\sqrt{2}s$. The largest scale used for the ε_k estimation is $s = 0.5$ s so the resolution is less than 1 s—that is, about 200 m on the horizontal and less than 7 m on the vertical.

Finally, we note that, in order to estimate ε_k , an alternative to the integrated variance approach used here is the maximum likelihood estimate from wind spectra (e.g., Sharman et al. 2014). Both methods give similar results for our dataset (not shown), consistent with the conclusions of Cornman (2016).

REFERENCES

- Abalos, M., W. J. Randel, D. E. Kinnison, and E. Serrano, 2013: Quantifying tracer transport in the tropical lower stratosphere using WACCM. *Atmos. Chem. Phys.*, **13**, 10591–10607, doi:10.5194/acp-13-10591-2013.
- Alappattu, D. P., and P. K. Kunhikrishnan, 2010: First observations of turbulence parameters in the troposphere over the Bay of Bengal and the Arabian Sea using radiosonde. *J. Geophys. Res.*, **115**, D06105, doi:10.1029/2009JD012916.
- Alexander, M. J., J. H. Beres, and L. Pfister, 2000: Tropical stratospheric gravity wave activity and relationships to clouds. *J. Geophys. Res.*, **105**, 22299–22309, doi:10.1029/2000JD900326.
- Alisse, J.-R., and C. Sidi, 2000: Experimental probability density functions of small-scale fluctuations in the stably stratified atmosphere. *J. Fluid Mech.*, **402**, 137–162, doi:10.1017/S0022112099006813.
- , P. H. Haynes, J. Vanneste, and C. Sidi, 2000: Quantification of stratospheric mixing from turbulence microstructure measurements. *Geophys. Res., Lett.*, **27**, 2621–2624, doi:10.1029/2000gl011386.
- Bacmeister, J. T., S. D. Eckermann, P. A. Newman, L. Lait, K. R. Chan, M. Loewenstein, M. H. Proffitt, and B. L. Gary, 1996: Stratospheric horizontal wavenumber spectra of winds, potential temperature, and atmospheric tracers observed by high-altitude aircraft. *J. Geophys. Res.*, **101**, 9441–9470, doi:10.1029/95JD03835.
- Balsley, B. B., 2008: The CIRES Tethered Lifting System: A survey of the system, past results and future capabilities. *Acta Geophys.*, **56**, 21–57, doi:10.2478/s11600-007-0045-z.
- Bardeen, C. G., A. Gettelman, E. J. Jensen, A. Heymsfield, A. J. Conley, J. Delano, M. Deng, and O. B. Toon, 2013: Improved cirrus simulations in a general circulation model using CARMA sectional microphysics. *J. Geophys. Res. Atmos.*, **118**, 11 679–11 697, doi:10.1002/2013JD020193.
- Bui, T., L. Pfister, S. W. Bowen, J. Dean-Day, and C. Chang, 2014: ATTREX meteorological measurement system data. NASA, accessed 9 September 2016, <https://espoarchive.nasa.gov/archive/browse/attrex>.

- Callies, J., R. Ferrari, and O. Bühler, 2014: Transition from geostrophic turbulence to inertia-gravity waves in the atmospheric energy spectrum. *Proc. Natl. Acad. Sci. USA*, **111**, 17 033–17 038, doi:10.1073/pnas.1410772111.
- Chan, K. R., J. Dean-Day, S. W. Bowen, and T. P. Bui, 1998: Turbulence measurements by the DC-8 Meteorological Measurement System. *Geophys. Res. Lett.*, **25**, 1355–1358, doi:10.1029/97GL03590.
- Cornman, L. B., 2016: Airborne in situ measurements of turbulence. *Aviation Turbulence*, R. Sharman and T. Lane, Eds., Springer, 97–120.
- , C. S. Morse, and G. Cuning, 1995: Real-time estimation of atmospheric turbulence severity from in-situ aircraft measurements. *J. Aircr.*, **32**, 171–177, doi:10.2514/3.46697.
- , G. Meymaris, and M. Limber, 2004: An update on the FAA Aviation Weather Research Program's in situ turbulence measurement and report system. *11th Conf. on Aviation, Range, and Aerospace Meteorology*, Hyannis, MA, Amer. Meteor. Soc., https://ams.confex.com/ams/11aram22sls/techprogram/paper_81622.htm.
- Dewan, E., 1981: Turbulent vertical transport due to thin intermittent mixing layers in the stratosphere and other stable fluids. *Science*, **211**, 1041–1042, doi:10.1126/science.211.4486.1041.
- Dole, J., R. Wilson, F. Dalaudier, and C. Sidi, 2001: Energetics of small scale turbulence in the lower stratosphere from high resolution radar measurements. *Ann. Geophys.*, **19**, 945–952, doi:10.5194/angeo-19-945-2001.
- ECMWF, 2009: ERA-Interim project. ECMWF Research Data Archive, accessed 20 September 2016, doi:10.5065/D6CR5RD9.
- Flannaghan, T. J., and S. Fueglistaler, 2014: Vertical mixing and the temperature and wind structure of the tropical tropopause layer. *J. Atmos. Sci.*, **71**, 1609–1622, doi:10.1175/JAS-D-13-0321.1.
- Fritts, D. C., L. Wang, J. Werne, T. Lund, and K. Wan, 2009: Gravity wave instability dynamics at high Reynolds numbers. Part II: Turbulence evolution, structure, and anisotropy. *J. Atmos. Sci.*, **66**, 1149–1171, doi:10.1175/2008JAS2727.1.
- Fueglistaler, S., A. E. Dessler, T. J. Dunkerton, I. Folkins, Q. Fu, and P. W. Mote, 2009: Tropical tropopause layer. *Rev. Geophys.*, **47**, RG1004, doi:10.1029/2008RG000267.
- Fukao, S., and Coauthors, 1994: Seasonal variability of vertical eddy diffusivity in the middle atmosphere: 1. Three-year observations by the middle and upper atmosphere radar. *J. Geophys. Res.*, **99**, 18 973–18 987, doi:10.1029/94JD00911.
- Gage, K. S., B. B. Balsley, and R. Garello, 1986: Comparisons of horizontal and vertical velocity spectra in the mesosphere, stratosphere and troposphere: Observations and theory. *Geophys. Res. Lett.*, **13**, 1125–1128, doi:10.1029/GL013i011p01125.
- Gini, C., 1921: Measurement of inequality of incomes. *Econ. J.*, **31**, 124–126, doi:10.2307/2223319.
- Glanville, A. A., and T. Birner, 2017: Role of vertical and horizontal mixing in the tape recorder signal near the tropical tropopause. *Atmos. Chem. Phys.*, **17**, 4337–4353, doi:10.5194/acp-17-4337-2017.
- Gultepe, I., and D. O. Starr, 1995: Dynamical structure and turbulence in cirrus clouds: Aircraft observations during fire. *J. Atmos. Sci.*, **52**, 4159–4182, doi:10.1175/1520-0469(1995)052<4159:DSATIC>2.0.CO;2.
- Jensen, E. J., L. Pfister, and O. B. Toon, 2011: Impact of radiative heating, wind shear, temperature variability, and microphysical processes on the structure and evolution of thin cirrus in the tropical tropopause layer. *J. Geophys. Res.*, **116**, D12209, doi:10.1029/2010JD015417.
- , and Coauthors, 2017: The NASA Airborne Tropical Tropopause Experiment (ATTREX): High-altitude aircraft measurements in the tropical western Pacific. *Bull. Amer. Meteor. Soc.*, **98**, 129–143, doi:10.1175/BAMS-D-14-00263.1.
- Kennedy, P. J., and M. A. Shapiro, 1975: The energy budget in a clear air turbulence zone as observed by aircraft. *Mon. Wea. Rev.*, **103**, 650–654, doi:10.1175/1520-0493(1975)103<0650:TEBIAC>2.0.CO;2.
- , and —, 1980: Further encounters with clear air turbulence in research aircraft. *J. Atmos. Sci.*, **37**, 986–993, doi:10.1175/1520-0469(1980)037<0986:FEWCAT>2.0.CO;2.
- Kim, J.-E., 2015: Impacts of atmospheric waves on tropical convection and the tropical tropopause layer. Ph.D. thesis, University of Colorado Boulder, 105 pp., http://scholar.colorado.edu/atoc_gradetds/53.
- , and M. J. Alexander, 2015: Direct impacts of waves on tropical cold point tropopause temperature. *Geophys. Res. Lett.*, **42**, 1584–1592, doi:10.1002/2014GL062737.
- Koch, S. E., and Coauthors, 2005: Turbulence and gravity waves within an upper-level front. *J. Atmos. Sci.*, **62**, 3885–3908, doi:10.1175/JAS3574.1.
- Konopka, P., and Coauthors, 2007: Contribution of mixing to upward transport across the tropical tropopause layer (TTL). *Atmos. Chem. Phys.*, **7**, 3285–3308, doi:10.5194/acp-7-3285-2007.
- Lane, T. P., and R. D. Sharman, 2006: Gravity wave breaking, secondary wave generation, and mixing above deep convection in a three-dimensional cloud model. *Geophys. Res. Lett.*, **33**, L23813, doi:10.1029/2006GL027988.
- , —, S. B. Trier, R. G. Fovell, and J. K. Williams, 2012: Recent advances in the understanding of near-cloud turbulence. *Bull. Amer. Meteor. Soc.*, **93**, 499–515, doi:10.1175/BAMS-D-11-00062.1.
- Legras, B., B. Joseph, and F. Lefèvre, 2003: Vertical diffusivity in the lower stratosphere from Lagrangian back-trajectory reconstructions of ozone profiles. *J. Geophys. Res.*, **108**, 4562, doi:10.1029/2002JD003045.
- Lilly, D. K., 1983: Stratified turbulence and the mesoscale variability of the atmosphere. *J. Atmos. Sci.*, **40**, 749–761, doi:10.1175/1520-0469(1983)040<0749:STATMV>2.0.CO;2.
- , D. E. Waco, and S. I. Adelfang, 1974: Stratospheric mixing estimated from high-altitude turbulence measurements. *J. Appl. Meteor.*, **13**, 488–493, doi:10.1175/1520-0450(1974)013<0488:SMEFHA>2.0.CO;2.
- Lindborg, E., 1999: Can the atmospheric kinetic energy spectrum be explained by two-dimensional turbulence? *J. Fluid Mech.*, **388**, 259–288, doi:10.1017/S0022112099004851.
- , 2006: The energy cascade in a strongly stratified fluid. *J. Fluid Mech.*, **550**, 207–242, doi:10.1017/S0022112005008128.
- Liu, C., E. J. Zipser, and S. W. Nesbitt, 2007: Global distribution of tropical deep convection: Different perspectives from TRMM infrared and radar data. *J. Climate*, **20**, 489–503, doi:10.1175/JCLI4023.1.
- Lovejoy, S., and D. Schertzer, 2011: Space-time cascades and the scaling of ECMWF reanalyses: Fluxes and fields. *J. Geophys. Res.*, **116**, D14117, doi:10.1029/2011JD015654.

- Lumley, J. L., 1964: The spectrum of nearly inertial turbulence in a stably stratified fluid. *J. Atmos. Sci.*, **21**, 99–102, doi:10.1175/1520-0469(1964)021<0099:TSOINT>2.0.CO;2.
- Mahoney, M. J., and R. Denning, 2009: A state-of-the-art airborne microwave temperature profiler (MTP). *Proceedings of the 33rd International Symposium on Remote Sensing of Environment: Sustaining the Millennium Development Goals*, ICRSE, 1306–1309.
- Mote, P. W., and Coauthors, 1996: An atmospheric tape recorder: The imprint of tropical tropopause temperatures on stratospheric water vapor. *J. Geophys. Res.*, **101**, 3989–4006, doi:10.1029/95JD03422.
- , T. J. Dunkerton, M. E. McIntyre, E. A. Ray, P. H. Haynes, and J. M. Russell, 1998: Vertical velocity, vertical diffusion, and dilution by midlatitude air in the tropical lower stratosphere. *J. Geophys. Res.*, **103**, 8651–8666, doi:10.1029/98JD00203.
- Nastrom, G. D., and K. S. Gage, 1985: A climatology of atmospheric wavenumber spectra of wind and temperature observed by commercial aircraft. *J. Atmos. Sci.*, **42**, 950–960, doi:10.1175/1520-0469(1985)042<0950:ACOAWS>2.0.CO;2.
- , D. C. Fritts, and K. S. Gage, 1987: An investigation of terrain effects on the mesoscale spectrum of atmospheric motions. *J. Atmos. Sci.*, **44**, 3087–3096, doi:10.1175/1520-0469(1987)044<3087:AIOTEO>2.0.CO;2.
- Osman, M., W. Hocking, and D. Tarasick, 2016: Parameterization of large-scale turbulent diffusion in the presence of both well-mixed and weakly mixed patchy layers. *J. Atmos. Sol.-Terr. Phys.*, **143–144**, 14–36, doi:10.1016/j.jastp.2016.02.025.
- Pavelin, E., J. A. Whiteway, R. Busen, and J. Hacker, 2002: Airborne observations of turbulence, mixing, and gravity waves in the tropopause region. *J. Geophys. Res.*, **107**, ACL 8-1–ACL 8-6, doi:10.1029/2001JD000775.
- Pellacani, C., and R. Lupini, 1975: Resonant trapped gravity waves and turbulent patches in an inversion layer. *Bound.-Layer Meteor.*, **9**, 205–215, doi:10.1007/BF00215640.
- Pfister, L., W. Starr, R. Craig, M. Loewenstein, and M. Legg, 1986: Small-scale motions observed by aircraft in the tropical lower stratosphere: Evidence for mixing and its relationship to large-scale flows. *J. Atmos. Sci.*, **43**, 3210–3225, doi:10.1175/1520-0469(1986)043<3210:SSMOBA>2.0.CO;2.
- Plougonven, R., A. Hertzog, and L. Guez, 2013: Gravity waves over Antarctica and the Southern Ocean: Consistent momentum fluxes in mesoscale simulations and stratospheric balloon observations. *Quart. J. Roy. Meteor. Soc.*, **139**, 101–118, doi:10.1002/qj.1965.
- Podglajen, A., A. Hertzog, R. Plougonven, and N. Žagar, 2014: Assessment of the accuracy of (re)analyses in the equatorial lower stratosphere. *J. Geophys. Res. Atmos.*, **119**, 112 166–112 188, doi:10.1002/2014JD021849.
- , —, —, and B. Legras, 2016a: Lagrangian temperature and vertical velocity fluctuations due to gravity waves in the lower stratosphere. *Geophys. Res. Lett.*, **43**, 3543–3553, doi:10.1002/2016GL068148.
- , R. Plougonven, A. Hertzog, and B. Legras, 2016b: A modelling case study of a large-scale cirrus in the tropical tropopause layer. *Atmos. Chem. Phys.*, **16**, 3881–3902, doi:10.5194/acp-16-3881-2016.
- Randel, W. J., M. Park, F. Wu, and N. Livesey, 2007: A large annual cycle in ozone above the tropical tropopause linked to the Brewer–Dobson circulation. *J. Atmos. Sci.*, **64**, 4479–4488, doi:10.1175/2007JAS2409.1.
- , R. Garcia, and F. Wu, 2008: Dynamical balances and tropical stratospheric upwelling. *J. Atmos. Sci.*, **65**, 3584–3595, doi:10.1175/2008JAS2756.1.
- Rao, D. N., T. N. Rao, M. Venkataratnam, S. Thulasiraman, S. V. B. Rao, P. Srinivasulu, and P. B. Rao, 2001: Diurnal and seasonal variability of turbulence parameters observed with Indian mesosphere-stratosphere-troposphere radar. *Radio Sci.*, **36**, 1439–1457, doi:10.1029/2000RS002316.
- Schmitt, F., D. Schertzer, S. Lovejoy, and Y. Brunet, 1994: Empirical study of multifractal phase transitions in atmospheric turbulence. *Nonlinear Processes Geophys.*, **1**, 95–104, doi:10.5194/npg-1-95-1994.
- Schneider, A., M. Gerding, and F.-J. Lübken, 2015: Comparing turbulent parameters obtained from LITOS and radiosonde measurements. *Atmos. Chem. Phys.*, **15**, 2159–2166, doi:10.5194/acp-15-2159-2015.
- Schumann, U., P. Konopka, R. Baumann, R. Busen, T. Gerz, H. Schlager, P. Schulte, and H. Volkert, 1995: Estimate of diffusion parameters of aircraft exhaust plumes near the tropopause from nitric oxide and turbulence measurements. *J. Geophys. Res.*, **100**, 14 147–14 162, doi:10.1029/95JD01277.
- Scott, S. G., T. P. Bui, K. R. Chan, and S. W. Bowen, 1990: The meteorological measurement system on the NASA ER-2 aircraft. *J. Atmos. Oceanic Technol.*, **7**, 525–540, doi:10.1175/1520-0426(1990)007<0525:TMMSOT>2.0.CO;2.
- Sharman, R. D., L. B. Cornman, G. Meymaris, J. Pearson, and T. Farrar, 2014: Description and derived climatologies of automated in situ eddy-dissipation-rate reports of atmospheric turbulence. *J. Appl. Meteor. Climatol.*, **53**, 1416–1432, doi:10.1175/JAMC-D-13-0329.1.
- Sreenivasan, K. R., 1991: Turbulence and stochastic processes: Kolmogorov's ideas 50 years on—On local isotropy of passive scalars in turbulent shear flows. *Proc. Roy. Soc. London*, **434A**, 165–182, doi:10.1098/rspa.1991.0087.
- , 1995: On the universality of the Kolmogorov constant. *Phys. Fluids*, **7**, 2778–2784, doi:10.1063/1.868656.
- Sunilkumar, S., and Coauthors, 2015: Characteristics of turbulence in the troposphere and lower stratosphere over the Indian Peninsula. *J. Atmos. Sol.-Terr. Phys.*, **133**, 36–53, doi:10.1016/j.jastp.2015.07.015.
- Theuerkauf, A., M. Gerding, and F.-J. Lübken, 2011: LITOS—A new balloon-borne instrument for fine-scale turbulence soundings in the stratosphere. *Atmos. Meas. Tech.*, **4**, 55–66, doi:10.5194/amt-4-55-2011.
- Thorpe, S. A., 1973: Turbulence in stably stratified fluids: A review of laboratory experiments. *Bound.-Layer Meteor.*, **5**, 95–119, doi:10.1007/BF02188314.
- Torrence, C., and G. P. Compo, 1998: A practical guide to wavelet analysis. *Bull. Amer. Meteor. Soc.*, **79**, 61–78, doi:10.1175/1520-0477(1998)079<0061:APGTWA>2.0.CO;2.
- Ueyama, R., E. J. Jensen, L. Pfister, and J.-E. Kim, 2015: Dynamical, convective, and microphysical control on wintertime distributions of water vapor and clouds in the tropical tropopause layer. *J. Geophys. Res. Atmos.*, **120**, 10 483–10 500, doi:10.1002/2015JD023318.
- Vanneste, J., 2004: Small-scale mixing, large-scale advection, and stratospheric tracer distributions. *J. Atmos. Sci.*, **61**, 2749–2761, doi:10.1175/JAS3303.1.
- Weinstock, J., 1978a: On the theory of turbulence in the buoyancy subrange of stably stratified flows. *J. Atmos. Sci.*, **35**, 634–649, doi:10.1175/1520-0469(1978)035<0634:OTTOTI>2.0.CO;2.

- , 1978b: Vertical turbulent diffusion in a stably stratified fluid. *J. Atmos. Sci.*, **35**, 1022–1027, doi:[10.1175/1520-0469\(1978\)035<1022:VTDIAS>2.0.CO;2](https://doi.org/10.1175/1520-0469(1978)035<1022:VTDIAS>2.0.CO;2).
- , 1992: Vertical diffusivity and overturning length in stably stratified turbulence. *J. Geophys. Res.*, **97**, 12 653–12 658, doi:[10.1029/92JC01099](https://doi.org/10.1029/92JC01099).
- Wilson, R., 2004: Turbulent diffusivity in the free atmosphere inferred from MST radar measurements: A review. *Ann. Geophys.*, **22**, 3869–3887, doi:[10.5194/angeo-22-3869-2004](https://doi.org/10.5194/angeo-22-3869-2004).
- , F. Dalaudier, and F. Bertin, 2005: Estimation of the turbulent fraction in the free atmosphere from MST radar measurements. *J. Atmos. Oceanic Technol.*, **22**, 1326–1339, doi:[10.1175/JTECH1783.1](https://doi.org/10.1175/JTECH1783.1).
- , —, and H. Luce, 2011: Can one detect small-scale turbulence from standard meteorological radiosondes? *Atmos. Meas. Tech.*, **4**, 795–804, doi:[10.5194/amt-4-795-2011](https://doi.org/10.5194/amt-4-795-2011).
- , H. Luce, H. Hashiguchi, N. Nishi, and Y. Yabuki, 2014: Energetics of persistent turbulent layers underneath mid-level clouds estimated from concurrent radar and radiosonde data. *J. Atmos. Sol.-Terr. Phys.*, **118A**, 78–89, doi:[10.1016/j.jastp.2014.01.005](https://doi.org/10.1016/j.jastp.2014.01.005).
- Wright, J. S., and S. Fueglistaler, 2013: Large differences in reanalyses of diabatic heating in the tropical upper troposphere and lower stratosphere. *Atmos. Chem. Phys.*, **13**, 9565–9576, doi:[10.5194/acp-13-9565-2013](https://doi.org/10.5194/acp-13-9565-2013).
- Wroblewski, D. E., O. R. Cot, J. M. Hacker, and R. J. Dobosy, 2010: Velocity and temperature structure functions in the upper troposphere and lower stratosphere from high-resolution aircraft measurements. *J. Atmos. Sci.*, **67**, 1157–1170, doi:[10.1175/2009JAS3108.1](https://doi.org/10.1175/2009JAS3108.1).